Masters thesis

Effective bond theory for frustrated magnets

Oliver Solow

Supervisor: Jens Paaske

Submitted: May 21, 2023

Contents

Abstract

Frustrated magnetic systems demonstrate a large range of different behaviors. This includes breaking of lattice symmetries, and phases characterized by strong short-range correlations without long-range symmetry breaking. The Nematic Bond Theory is a tool for studying classical frustrated magnets described by the Heisenberg model. We demonstrate a derivation of Nematic Bond Theory in the case of non-Bravais lattices, and we extend the theory to be able to compute the specific heat of the magnetic system. We then use this theory to explore a number of different systems. We explore the honeycomb lattice with up to third-nearest neighbor couplings, and show that the the nematic order manifests in qualitatively different ways at different phase boundaries. We then turn to the triangular lattice with a long-range RKKY interaction. We show that this system demonstrates spin-liquid behavior near the ferromagnetic-nematic phase boundary, and that it demonstrates an unusually high critical temperature near the nematic-120° phase boundary. We link this unusually high critical temperature to features in the specific heat of the system, and find a similar phenomenon in the triangular lattice with up to third-nearest neighbor couplings.

When deriving the Nematic Bond Theory, we neglect the vertex correction. We demonstrate that for Bravais lattices with short-range couplings, neglecting the vertex correction is a good approximation. For non-Bravais lattices, we demonstrate that the vertex correction cannot in general be neglected.

Acknowledgements

Chapter 1

Introduction

In magnetic materials, order comes about due to the interaction between magnetic moments. In frustrated magnets, these interactions compete in such a way that their energies cannot all be minimized simultaneously. Thus, the system seeks out a "compromise" state. This in turn leads to a number of interesting phenomena, including complex magnetic order and the presence of spin-liquid phases described by emergent theories [1]. Both classical and quantum magnetic materials host a wide variety of phases. In quantum magnets, entanglement between the spins leads to a wide range of possible states, including states with interesting topological properties. The classical models also demonstrate a wide variety of states, including non-trivial ordered states and classical spin liquids with large short-range correlations. In addition, the classical spin models are important precursors to understanding the quantum models.

To understand classical spin models, a number of methods are used, including Monte Carlo. Many of these methods suffer from being computationally expensive as the size of the system is increased, and as such they are ill-suited to treat large systems. This makes the treatment of long-range order particularly difficult.

Another approach to understanding classical spin models is the Nematic Bond Theory (NBT) [2]. This theory converts the problem of finding the state of the system into a field-theoretical problem, which is in turn solvable by using diagrammatic methods as we know them from quantum field theory. This allows us to efficiently find the approximate state of the system by performing certain approximations in the diagrammatic language of the theory.

In this thesis, we will extend the Nematic Bond Theory allow it to compute the heat capacity, thus giving us a new measurable property that we can compute. We will then apply Nematic Bond Theory to two systems where it has not been applied before. In particular, for the honeycomb lattice we will extend it to up to third-nearest neighbor couplings, which opens up a rich phase diagram with several complex phases and phase transitions. For the triangular lattice, we will introduce long-range interactions. We will

observe a number of unexpected phenomena, which demonstrate the complexity of these frustrated systems and the need for further computational methods.

We will also discuss whether Nematic Bond Theory is on solid theoretical footing. In particular, we will analyze whether the approximations made when deriving it are valid, and see that the approximations are valid in some regimes.

The thesis is structured as follows:

- In chapter 2, we will go through some of the background of frustrated magnets. We will discuss the definition of frustration in magnetic systems, and the nature of magnetic phase transitions in general with a focus on the nematic phase.

- In chapter 3, we will derive Nematic Bond Theory for an arbitrary inversion-symmetric lattice. This derivation is then followed by a description of how NBT is implemented numerically. We also describe how this implementation can be used to compute the specific heat of a spin model.

- In chapter 4, the honeycomb lattice with up to third-nearest neighbor couplings and the triangular lattice with long-range coupling are described. NBT is applied to compute the states of both lattices for various temperatures and coupling strengths. For the honeycomb lattice, we look at the different phase boundaries between nematic and non-nematic phases. We show that the critical temperature as a function of the interaction strengths behaves quantitatively differently at different phase boundaries. For the triangular lattice, we show that long-range order induces a number of unexpected behaviors. To understand whether this is physical, we compare these behaviors with similar behaviors found on the triangular lattice with up to third-nearest neighbor couplings. We see that the behavior is indeed physical.

- In chapter 5, we discuss to what extent our results are valid, taking into account the approximations required to derive NBT, as well as the difference between our model and real magnetic materials. We also discuss some of the results from chapter 4, as well as why NBT fails in certain situations.

- In chapter 6, we summarize the findings of the thesis. We then describe the various directions that further research could take.

Chapter 2

Interactions and structures

In this chapter, I will introduce a number of background concepts for the understanding of magnetic materials generally and frustrated magnets in particular.

2.1 Magnetic moments

In this thesis, we will study materials whose magnetic properties come from localized magnetic moments. These localized moments are caused by the electron structure of atoms within the material. The electrons generate a magnetic moment in two ways: Through their own intrinsic magnetic moment, and through their orbital motion, which provides a magnetic moment if the electron has a non-zero angular momentum. These two moments then add up to cause the overall magnetic moment of the ion. Depending on the number of electrons, the different contributions from each electron might cancel out, or they might add up. The rules for determining to what extent they cancel out or add up are called Hund's rules [3].

As a very general rule of thumb, a magnetic moment is most likely present in metallic ions. Most magnetic material gain their magnetic moment from transition metals like iron, nickel, cobalt and chromium.

A magnetic material is also likely to contain non-magnetic ions, like oxygen. While these non-magnetic ions can have a large effect on the structure of the material and the interaction between magnetic ions, all of these effects can be abstracted into parameters of our model like the coupling strengths J_i and the lattice constants a_i. As such, we can ignore the presence of these non-magnetic ions when developing our theory.

Not all magnetism is caused by localized magnetic moments. In some materials, the magnetism is instead caused by the conductance electrons. These so-called itinerant magnets are fascinating in their own right, but their description is made significantly more complex by the interplay of magnetic and electronic factors.

Spin is a quantum mechanical property, and is characterized by spin operators $\vec{\mathbf{S}}$ and

spin quantum numbers s and m. Doing computations with these quantum operators is difficult, however, as the spin operators do not obey nice (anti)commutator relations like bosons and fermions. As such, they require special care. A variety of techniques exist to work with them. In this thesis, however, we will simply treat the spins as classical dipoles, i.e classical vectors. This is approximately true for large s in many cases. Due to this connection with the quantum mechanical spins, we will describe the magnetic moments of our ions as "spins".

2.2   Magnetic interactions

The theory we will be working with, Nematic Bond Theory, is a theory for analyzing Hamiltonians of the form

$$H = \frac{1}{2} \sum_{i,j} J_{ij} \vec{S}_i \cdot \vec{S}_j \tag{2.1}$$

with no other interactions present. The name of this Hamiltonian depends on how many dimensions the spin has: The 1d case is called the Ising model, the 2d case is called the XY model, and the 3d case is called the Heisenberg model, which is the main model that we will study. While the form of the Hamiltonian excludes certain interactions, there are at least two prominent physical interactions with this form: The exchange interaction and the RKKY interaction.

The exchange interaction is one of the primary mechanism by which materials develop magnetic order. It comes about due to the combination of two factors: The Pauli exclusion principle and the Coulomb repulsion. Specifically, the Pauli exclusion principle demands that the wavefunction of any pair of electrons changes sign when the electrons are exchanged. As the wavefunction has both a location component and a spin component, the sign change can happen in either, and as such this principle couples the spin of the electron to its wavefunction. The Coulomb repulsion between electrons then cause the electrons to choose the wavefunction where they stay as far away from each other as possible. If this wavefunction is even, the spin state must be odd and the electrons must form a singlet, while if the location wavefunction is odd, the spins must be even and in a triplet. Thus, we get an interaction between the spins [4].

This interaction is relevant in two cases. In the case of direct exchange, the electron orbitals of two atoms with non-zero magnetic moment overlap, and as such the electrons have a significant interaction. This, however, is somewhat rare. A more common situation is where the exchange interaction between two magnetic atoms is mediated by a third, non-magnetic atom, often oxygen. This is called superexchange [4].

The exchange interaction depends on the orbitals of the interacting atoms to overlap, or at least for there to be a mediating atom in between. As such, it is a relatively short-ranged interaction. A much longer-ranged interaction which also has the correct form is

the RKKY interaction. This interaction depends on the presence of delocalized electrons. These electrons can be polarized by a magnetic moment, and then interact with other magnetic moments in the material, which leads to an effective spin-spin interaction which depends on the distance between the atoms. This interaction is oscillatory, and can either cause the magnetic moments to align or to anti-align depending on the distance. The RKKY interaction is most common in cases of diluted magnetic ions in a conductor, or magnetic ions deposited on the surface of a conductor. However, there are also materials where the RKKY interaction is believed to be the primary interaction between the magnetic ions in the crystal lattice [5].

The form of the RKKY interaction depends on the geometry of the Fermi surface of the material. For a spherical Fermi surface in 3d, the RKKY interaction has the form [4]

$$J(r) = J \left(\frac{\cos(2k_F r)}{(2k_F r)^3} - \frac{\sin(2k_F r)}{(2k_F r)^4} \right) \tag{2.2}$$

where k_F is the Fermi momentum of the polarized electrons and J is a coupling constant which depends on the details of the system. The RKKY interaction is interesting because the interaction strength goes as $\frac{1}{r^3}$ for large r. This means that the interaction is in principle infinitely-ranged, and is very different from the short-ranged exchange interaction. This longer range also makes this interaction more difficult to understand with Monte Carlo methods, making it a prime candidate for a different numerical approach.

2.3 Frustration

We describe a magnetic material as being frustrated when competing interactions cannot simultaneously be satisfied. The canonical example of this is three spins on the corners of a triangle, with a coupling that minimizes the energy when the spins anti-align. Of course, three spins cannot simultaneously be anti-aligned, and as such the "optimal" ground state does not exist. For the system of three spins, the ground state is one where they are 120° rotated from each other.

Many different lattices contain clusters of three nearest-neighbor spins which are all coupled, and these can display frustration. Since the frustration is caused by the geometry of the lattice, it is referred to as geometric frustration. This occurs whenever there is a odd cycle in the lattice with anti-aligning coupling all along the cycle. The most common case is a lattice which contains triangles, but some lattices can also contain pentagons [6]. Frustration can also be caused by different types of interaction. If a lattice both have nearest-neighbor and next-nearest-neighbor couplings, for example, these two different couplings can compete and lead to frustration. In general, frustration can be caused by longer range coupling since these potentially cause the spins to want to be anti-aligned with many other spins.
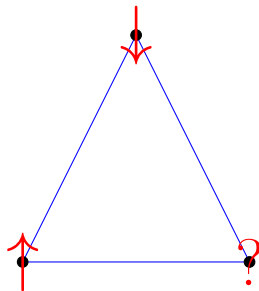
Figure 2.1: A triangle with antiferromagnetic coupling between the spins on each corner. All three spins cannot simultaneously be anti-aligned.

This kind of frustration requires the presence of significant long-range interaction. As most interactions are exchange interactions mediated by atomic orbitals, it is relevant to ask whether any real-life materials display strong long-range interactions. Fortunately, there are several examples of materials with long-range interactions which are as strong or even stronger than the nearest-neighbor interaction. One such example is NiS_2 [7], a material in which the magnetic Ni ions form a hexagonal lattice. In this material, the third-neighbor interaction between the nickel atoms, mediated by superexchange through a sulfur atom, is significantly stronger than the nearest and next-nearest interactions. This shows that long-range coupling is possible even using the normally short-ranged exchange coupling. In addition, couplings like the RKKY coupling also yield long-range interactions. In frustrated compounds, the interplay of various interactions often leads to very complex behavior. Even in the relatively simple case of classical magnets with no external magnetic field, which is what we are studying, several exotic phases of matter occur. To understand these, we need to understand how magnetic materials work in more general terms.

2.4   Magnetic order

When the spins in a material interact, they can develop magnetic order. Simply put, magnetic order means that the direction of the spins is aligned in some pattern, such that by knowing the direction of one spin you can predict the direction of other spins. The most well known case is ferromagnetism, where the spins in a lattice are all aligned the same way. In a ferromagnet, the magnetic fields all add up, and thus the material has a macroscopic magnetic field.

A slightly more complex case is the antferromagnet. In an antiferromagnet, each spin points opposite of its neighbors. As such, there is no net magnetic field. There is still a large degree of ordering, however, and as such this phase can be readily seen by neutron

scattering. We also use the terms ferromagnetic and antiferromagnetic to describe the interaction between two spins, depending on whether the interaction causes the two spins to align or to antialign.

When ferromagnetic or antiferromagnetic order develops, there is spontaneous breaking of the symmetry of the spins. Indeed, the ferromagnetic transition is the quintessential example of spontaneous symmetry breaking; the system chooses a direction to point all of the spins, and thus breaks the symmetry of the spins. The symmetry which is broken here is a continuous symmetry, it is $O(3)$ symmetry for the Heisenberg model and $O(2)$ for the XY model. Thus, these symmetry breakings are governed by the Mermin-Wagner theorem.

The Mermin-Wagner theorem states that continuous symmetries cannot be spontaneously broken in less than 3 dimension [8]. As we primarily look at 2d systems in this thesis, that precludes the breaking of spin symmetry. Thus, if we have phase transitions the broken symmetries cannot be continuous, and must be discrete. Frustrated magnets can have these discrete symmetries. To see this, it is instructive to look at a particular generalization of the ferromagnetic and antiferromagnetic states that we have considered. We can consider the so-called spiral states. These states are given as

$$\vec{S}(\vec{r}) = \vec{u}\cos\left(\vec{r}\cdot\vec{Q}\right) + \vec{v}\sin\left(\vec{r}\cdot\vec{Q}\right) \tag{2.3}$$

where $\vec{u}$ and $\vec{v}$ are two arbitrary unit vectors and $\vec{Q}$ is the so-called ordering vector of the system. The ordering vector is found by finding the minima of $J_{\vec{q}}$, which is the spin coupling in reciprocal space. It is possible to prove that at least one of the ground states of the Heisenberg model for any periodic J_{ij} is a spiral state [9]. For example, the ferromagnetic state is a spiral state with $\vec{Q} = (0,0)$, while the antiferromagnetic state in a square lattice is given by $\vec{Q} = (\pi,\pi)$.

There can be several minima of $J_{\vec{q}}$. We define the star of $\vec{Q}$ as the set of minima which are not connected to each other by a reciprocal lattice vector [9]. Those minima which are connected by a reciprocal lattice vector lead to the same physical spin configuration, and are thus said to be equivalent. In addition, the states given by $\vec{Q}$ and $-\vec{Q}$ are related by a global spin rotation, and thus are not distinct states either. For the ferromagnet and antiferromagnet, the star of $\vec{Q}$ only contains one element. For more complicated order, the star of $\vec{Q}$ might contain several elements. For example, it could contain the elements $\vec{Q} = (0,\pi)$ and $\vec{Q} = (\pi,0)$. These elements are usually related by a lattice symmetry, but as they are not connected by a reciprocal lattice vector they describe distinct state. Thus, the system has multiple spiral ground states. Since the symmetry between these ground states is discrete, the Mermin-Wagner theorem does not apply, and as such the symmetry can be spontaneously broken above $T = 0$.

While the star of $\vec{Q}$ can be composed of high-symmetry points in the Brillouin zone, it can also be composed of any arbitrary points within the Brillouin zone. The states associated

with these non-symmetry points of the Brillouin zone are called incommensurate spiral states. In an incommensurate state, the rotation angle between neighboring spins is not π or 0.

One final possibility is when the star of $\vec{Q}$ is a continuous set. For example, the star of $\vec{Q}$ can form a closed curve around a high-symmetry point. These cases are somewhat more complicated, and can lead to a variety of different states depending on the details of the system. We will not be encountering many situations where this is the case.

2.5 Phase transition

A phase transition is linked to the breaking of a discrete or continuous symmetry[1]. Since such a symmetry is either broken or not, there must be some kind of discontinuity at the transition point. The nature of this discontinuity depends on the phase transition.

The free energy is always continuous, but at the phase transition it is not necessarily smooth. Thus, the type of phase transition can be determined by the differentiability of the derivative of the free energy. A first-order phase transition is one where the first derivative of the free energy is discontinuous. In these phase transitions, there is a non-zero energy barrier going between the symmetric and non-symmetric state, and thus there are metastable states where the symmetric state can be maintained below the transition temperature. An example of such a phase transition is the freezing of water. A phase transition can also be second-order, meaning that the second derivative of the free energy is discontinuous, but the first derivative is continuous. Such a phase transition does not have metastable states.

To quantify these phase transitions, we can introduce so-called order parameters. An order parameter is some quantity which is zero above the transition temperature and non-zero below the transition temperature. An example is the net magnetization, which is zero for a paramagnet but non-zero for a ferromagnet. The order parameter is usually a first derivative of the free energy, and thus its continuity depends on the nature of the phase transition.

In this thesis, we will be studying the breaking of the symmetry between discrete ground states described above. This phase transition is called a lattice-nematic phase transition, or simply a nematic phase transition. We can define a nematic order parameter, which will quantify to what degree the correlations in one direction are larger than those in another direction. The exact definition of the nematic order parameter depends on the lattice and nematic symmetry in question, but it is generally defined by assigning each $\vec{Q}$ a complex root of unity, which ensures that if the correlation in each $\vec{Q}$-direction is equal,

---

[1]This does not apply to topological phase transitions, like the BKT transition. We will not be looking at any topological phase transition, in part because the method we will develop does not capture these transitions well.

the roots of unity will cancel out, while if the correlation varies the order parameter will be finite.

In general, one would expect that the transition temperature of this nematic phase is on the order of the energy barrier between the elements of the star of $\vec{Q}$. If we think of thermal fluctuations perturbing the system around a spiral ground state, we expect the transition when there is enough energy in the fluctuations to push the system above the energy barrier. There are cases where this is not the whole story, however. One example is when the star of $\vec{Q}$ is a continuous set. In this case, the continuous degeneracy can be lifted by thermal fluctuations. In other words, while there are a continuous set of $\vec{Q}$ which minimize the energy E, not all of them minimize the free energy $F = E - TS$. This phenomenon is called order by disorder [10].

2.6 Spin Liquid

Not all magnetic behavior is explained by ordering or symmetry breaking. Instead, the magnetic phase known as a spin liquid is a significantly more diffuse topic. A spin liquid is generally defined as a state where the spins are strongly correlated but do not break any lattice symmetries [1]. The physics of these spin liquids is governed by various emergent theories which take into account the strong correlations between the spins and describe the effective degrees of freedom of the model. The canonical example is spin ice, which is described by a gauge theory similar to electromagnetism [11]. In many of the systems which have been analyzed before, the spin liquid behavior is related to a macroscopically degenerate ground state, which can for example be seen in the honeycomb lattice with nearest-neighbor and next-nearest neighbor couplings [12]. In terms of $\vec{Q}$, this is the situation where the star of $\vec{Q}$ formed a closed curve around a high-symmetry point.

Even in the classical case, spin liquids are complex, with some being well-described by gauge theories or other emergent theories. For quantum spins, the situation becomes much more complicated, with many types of spin-liquids emerging around critically frustrated points. Here, the behavior is much less well-understood than for classical spins. In the case of the square lattice with $J_2 \approx \frac{J_1}{2}$, usually considered one of the simplest cases of frustration, there is still debate around the exact nature of the spin liquid [13].

Chapter 3

Nematic bond theory

Nematic Bond Theory (NBT) is an approach to treat classical frustrated magnets. This method is similar to the Self-Consistent Gaussian Approximation (SCGA) [14], but unlike SCGA, Nematic Bond Theory does not require the found state to obey any of the symmetries of the point group of the lattice. The only requirement of the lattice is that it obeys inversion symmetry. The theoretical framework of Nematic Bond Theory uses the tools of statistical field theory, which allows us to use the full machinery of quantum field theory to treat problems in statistical physics. However, it is important to keep in mind that the system that we are working with is still classical.

The major advantage of Nematic Bond Theory over Monte Carlo methods is that it is much faster for large systems. Being able to do computations on larger systems allows us to analyze long-range interactions without worrying about boundary effects. In addition, this allows us to search through a large parameter space without requiring huge amounts of computational resources.

Here, we will derive Nematic Bond Theory for an arbitrary inversion-symmetric lattice, following [15]. We will also discuss some of the approximations made in the theory, and to what extend they are valid.

Several times during this derivation, constant factors will be absorbed into the integration measure. These constant factors do end up being relevant, and are thus restored at the end of the derivation.

3.1 Field theory of the Heisenberg model

Our derivation starts with the Hamiltonian of the Heisenberg model:

$$H = \frac{1}{2} \sum_{\vec{r}\vec{r}'} \sum_{ij} J_{\vec{r}\vec{r}'ij} \vec{S}_{\vec{r},i} \cdot \vec{S}_{\vec{r}',j} \tag{3.1}$$

Where $\vec{r}$ and $\vec{r}'$ denote the unit cells and i and j are sublattice indices within the unit cell. $J_{\vec{r}\vec{r}'ij}$ is the interaction between the spins $\vec{S}_{\vec{r},i}$ and $\vec{S}_{\vec{r}',j}$, which depends on the exact

details of the underlying physics. The sublattices notation is a way to describe a non-Bravais lattice as a combination of a basis and an underlying Bravais lattice [16], which simplifies calculations.

The partition function can be written as

$$Z = \int D\vec{S} e^{-\beta H} \tag{3.2}$$

Here, it is worth being explicit about the integration measure. Since the size of the spins is determined by electronic effects that are not changed by our magnetic interactions, the length of the spins is constant, and can be set to 1 for convenience. This means that the integral is only over configurations where the length of the spin is constant. As such, even though the Hamiltonian is quadratic in spins, this is not a Gaussian integral, and it cannot be solved easily. We can change the integration measure to include spin configurations with varying-length spins, if we simultaneously multiply our integrand by delta functions to ensure that we still only count contributions from configurations with unit-length spins:

$$Z = \int D\vec{S} e^{-\beta H} \delta(\vec{S}_{\vec{r},i}^2 - 1). \tag{3.3}$$

We can then use the identity

$$\delta(\vec{S}_{\vec{r},i}^2 - 1) = \int \frac{\beta d\lambda_{\vec{r},i}}{2\pi} e^{-i\beta\lambda_{\vec{r},i}(\vec{S}_{\vec{r},i}^2 - 1)}$$

to write the partition function. Transforming everything to reciprocal space, we get

$$Z = \int D\vec{S} D\lambda e^{-\beta\left(J_{\vec{q},ij}\delta_{\vec{q}\vec{q}'} + i\frac{1}{\sqrt{V}}\lambda_{\vec{q}-\vec{q}'}\delta_{ij}\right)\vec{S}_{\vec{q},i}\cdot\vec{S}_{\vec{q}',j}} e^{-i\beta\sqrt{V}\lambda_{\vec{q}=0,i}} \tag{3.4}$$

where V is the number of unit cells, which we think of as the volume, and all constant factors have been absorbed into the integration measures. Without any loss of generality, we can define $J_{\vec{q},ij}$ such that its minimal eigenvalue is zero. We now see that we have the desired quadratic action in $\vec{S}$, and so we can perform that integral. If we scale the spins by $\frac{1}{\sqrt{\beta}}$ and perform the integral, we get:

$$Z = \int D\lambda e^{-\frac{N}{2}\operatorname{Tr}\ln(\mathbf{J}+\mathbf{\Lambda}) - i\beta\sqrt{V}\sum_i \lambda_{\vec{q}=0,i}} \tag{3.5}$$

where we have defined tensors $\mathbf{J}_{\vec{q}\vec{q}',ij} = J_{\vec{q},ij}\delta_{\vec{q}\vec{q}'}$ and $\mathbf{\Lambda}_{\vec{q}\vec{q}',ij} = i\frac{1}{\sqrt{V}}\lambda_{q-q',i}\delta_{ij}$, and we have absorbed all constant factors into the integration measures. In general, we let bold symbols refer to objects with four total indices: two momentum indices and two sublattice indices.

We now want to consider how to perform the integral over λ. To perform this integral, we will make a saddle point approximation of a spatially homogenous λ, and then expand around this saddle point. It is worth thinking about what this means physically. The λ

field carries information about the constraint on the spins, so we can label it a constraint field. Thus, we are approximating the constraint as being homogenous, which is equivalent to the softer constraint

$$\frac{1}{V}\sum_{\vec{q}}\langle \vec{S}_{\vec{q},i}\cdot \vec{S}_{-\vec{q},i}\rangle = 1. \tag{3.6}$$

This is where the similarity to the Self-Consistent Gaussian Approximation comes in, as it also uses a homogenous saddle point. The difference between our method and the SCGA is that while the SCGA neglects the non-homogeneous part of the constraint, we will include them, as these non-homogeneous fluctuations around the saddle point are then what leads to the symmetry-breaking in the nematic phase.

We introduce the saddle point by defining

$$\Delta_i = i\frac{1}{\sqrt{V}}\lambda_{\vec{q}=0,i}. \tag{3.7}$$

We can thus write $\lambda_{\vec{q},i} = -i\sqrt{V}\Delta_i\delta_{\vec{q}} + \sqrt{V}\tilde{\lambda}_{\vec{q},i}$ where we have separated the constraint field into a homogeneous part and a non-homogeneous part $\tilde{\lambda}_{\vec{q}}$, which we can define such that $\tilde{\lambda}_{\vec{q}=0} = 0$. We can then write the effective action we have as

$$S[\tilde{\lambda},\Delta] = \frac{N}{2}\operatorname{Tr}\ln\left(\mathbf{J} - \tilde{\mathbf{\Lambda}} + \mathbf{\Delta}\right) - \beta V\sum_i \Delta_i \tag{3.8}$$

where $\mathbf{\Delta}_{\vec{q}\vec{q}',ij} = \Delta_i\delta_{ij}\delta_{\vec{q}\vec{q}'}$ and $\tilde{\mathbf{\Lambda}}_{\vec{q}\vec{q}',ij} = -i\tilde{\lambda}_{q-q',i}\delta_{ij}$.

We will refer to $\tilde{\mathbf{\Lambda}}$ as the constraint field from now on, as it still carries a significant part of the constraint. We can now expand the action in powers of $\tilde{\mathbf{\Lambda}}$. To do this, we define $\mathbf{K} = \mathbf{J} + \mathbf{\Delta}$. The action can then be Taylor expanded as

$$S[\tilde{\lambda},\Delta] = \frac{N}{2}\operatorname{Tr}\ln\mathbf{K} - \frac{N}{2}\sum_{j\geq 2}\frac{1}{j}\operatorname{Tr}\left(\tilde{\mathbf{\Lambda}}\mathbf{K}^{-1}\right)^j - \beta V\sum_i \Delta_i. \tag{3.9}$$

3.1.1 Diagrams

The most important property that we want to be able to compute is the spin correlation function $\langle \vec{S}_{\vec{q},i}\cdot \vec{S}_{-\vec{q},j}\rangle$. This is equal to the susceptibility, and contains much of the information about the spin configuration, including symmetry properties. From (3.8), we see that the spin correlation can be written as

$$\langle \vec{S}_{\vec{q},i}\cdot \vec{S}_{-\vec{q},j}\rangle = \frac{NT}{2}\left\langle \left(\mathbf{K} - \tilde{\mathbf{\Lambda}}\right)^{-1}_{\vec{q}\vec{q},ij}\right\rangle = \frac{NT}{2}K_{\text{eff}\,\vec{q},ij}^{-1} \tag{3.10}$$

where we have defined the effective spin propagator $K_{\text{eff}\,\vec{q},ij}$, and the T comes from our rescaling of the spins to perform the integral leading to (3.8). We can now Taylor expand this effective propagator in terms of $\tilde{\lambda}$:

$$K_{\text{eff}\,\vec{q},ij}^{-1} = \left\langle \left[\left(\mathbf{1} - \tilde{\mathbf{\Lambda}}\mathbf{K}^{-1}\right)^{-1}\mathbf{K}^{-1}\right]_{\vec{q}\vec{q},ij}\right\rangle = K_{\vec{q},ij}^{-1} + \left\langle \sum_{n=1}^{\infty}\left[\left(\mathbf{K}^{-1}\tilde{\mathbf{\Lambda}}\right)^n\mathbf{K}^{-1}\right]_{\vec{q}\vec{q},ij}\right\rangle \tag{3.11}$$

where $K_{\vec{q},ij} = J_{\vec{q},ij} + \Delta_i \delta_{ij}$ is the zero-order term in $\tilde{\lambda}$ and the other term is the correction from $\tilde{\lambda}$. We can now define

$$K_{\vec{q},ij}^{-1} = \quad i \xrightarrow{\quad q \quad} j \tag{3.12}$$

Building this diagrammatic language, we can write the terms in the sum in this form:

$$[\mathbf{K}^{-1}\tilde{\mathbf{\Lambda}}\mathbf{K}^{-1}\tilde{\mathbf{\Lambda}}\mathbf{K}^{-1}]_{\vec{q}\vec{q},ij} = \quad i \xrightarrow{q}\zeta \underset{\longrightarrow}{} \zeta\xrightarrow{q} j \tag{3.13}$$

where the wiggly lines represent the $\tilde{\mathbf{\Lambda}}$ terms. We note that each $\tilde{\mathbf{\Lambda}}$ contains a factor of $-i$, and as thus each vertex carries a $-i$.

We now need to take the expectation value of these terms. The expectation value of an operator is defined as

$$\langle \ldots \rangle = \frac{\int D\tilde{\lambda} \ldots e^{-S[\tilde{\lambda},\Delta]}}{\int D\tilde{\lambda} e^{-S[\tilde{\lambda},\Delta]}}. \tag{3.14}$$

Since $\mathbf{K}$ does not depend on $\tilde{\lambda}$, the challenging part is to find the expectation value of products of $\tilde{\lambda}$. This expectation value depends on the $\tilde{\lambda}$-dependent part of the action, which is composed of the series

$$S_\lambda = -\frac{N}{2} \sum_{j \geq 2} \frac{1}{j} \operatorname{Tr}\left(\tilde{\mathbf{\Lambda}}\mathbf{K}^{-1}\right)^j.$$

We note that the first term in this series leads to a Gaussian term in the partition function:

$$S_2 = \frac{1}{2} \sum_{\vec{q}} \sum_{ij} \tilde{\lambda}_{-\vec{q},i} \left[\frac{N}{2} \sum_{\vec{p}} K_{\vec{q}+\vec{p},ij}^{-1} K_{\vec{p},ji}^{-1} \right] \tilde{\lambda}_{\vec{q},j}. \tag{3.15}$$

We can thus define

$$D_{0\vec{q},ij} = \left[\frac{N}{2} \sum_{\vec{p}} K_{\vec{q}+\vec{p},ij}^{-1} K_{\vec{p},ji}^{-1} \right]^{-1} = \quad i \xrightarrow{\quad q \quad}_{\sim\sim\sim\sim} j \, . \tag{3.16}$$

As this term comes from the Gaussian part of the $\tilde{\lambda}$ terms, it is in a sense the "bare" propagator for the constraint field. In other words, we can write the full propagator for the constraint field as

$$D_{\vec{q},ij} = \langle \tilde{\lambda}_{\vec{q},i} \tilde{\lambda}_{-\vec{q},j} \rangle = D_{0\vec{q},ij} + \frac{1}{Z} \int D\tilde{\lambda} \mathcal{O}(\tilde{\lambda}^3) = \quad i \xrightarrow{\quad q \quad}_{\sim\sim\sim\sim} j \tag{3.17}$$
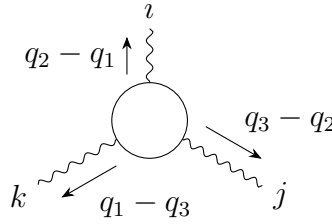
Of course, the natural question is what the higher order contributions are. To understand this, we need to look at the remaining part of the action. These remaining terms have the form

$$S_j = -\frac{N}{2}\frac{1}{j} \operatorname{Tr}\left(\tilde{\mathbf{\Lambda}}\mathbf{K}^{-1}\right)^j$$

17

If we consider the $j = 3$ term, we can write it as:

$$S_3 = -\frac{N}{2}\frac{1}{3}\text{Tr}\left(\tilde{\mathbf{\Lambda}}\mathbf{K}^{-1}\tilde{\mathbf{\Lambda}}\mathbf{K}^{-1}\tilde{\mathbf{\Lambda}}\mathbf{K}^{-1}\right)$$

$$= -(-i)^3\frac{N}{2}\frac{1}{3}\sum_{\vec{q}_1,\vec{q}_2,\vec{q}_3}\sum_{ijk}K^{-1}_{\vec{q}_1,ki}\tilde{\lambda}_{\vec{q}_2-\vec{q}_1,i}K^{-1}_{\vec{q}_2,ij}\tilde{\lambda}_{\vec{q}_3-\vec{q}_2,j}K^{-1}_{\vec{q}_3,jk}\tilde{\lambda}_{\vec{q}_1-\vec{q}_3,k}$$

(3.18)

which can be written diagramatically as

(3.19)

where we have omitted writing the internal momenta. For the purposes of simplifying the diagrammatic notation, we will omit writing the momenta and sublattice indices unless required.

What we see here is that the higher-order terms in $\tilde{\lambda}$ are loops with j "hooks". Thus, these loops become an essential part of our theory, obeying the rules that

1. Only loops with at least three $\tilde{\lambda}$ exist, the two-$\tilde{\lambda}$ loop has been absorbed into the bare constraint propagator.

2. Each loop contributes a factor of $\frac{N}{2}\frac{1}{j}$ where j is the number of $\tilde{\lambda}$ terms.

Taking the expectation value of a term like $[\mathbf{K}^{-1}\tilde{\mathbf{\Lambda}}\mathbf{K}^{-1}\tilde{\mathbf{\Lambda}}\mathbf{K}^{-1}]_{\vec{q}\vec{q},ij}$, the term in eq. (3.13), is then equivalent to connecting all $\tilde{\lambda}$ in the expression with propagators $D_{\vec{q},ij}$, which are in turn composed of combinations of the "bare" propagators $D_{0\vec{q},ij}$ and loops with at least three hooks, which obey the rules given above. As a very simple example, we can look at $D_{\vec{q},ij}$ itself, which is the expectation value $\langle\tilde{\lambda}_{\vec{q},i}\tilde{\lambda}_{-\vec{q},j}\rangle$:

$$D_{\vec{q},ij} = \langle\tilde{\lambda}_{\vec{q},i}\tilde{\lambda}_{-\vec{q},j}\rangle = \text{\small〜〜〜} = \text{\small〜〜〜} + \text{\small〜O〜} + \text{\small〜⊗〜} + \text{\small⊃O⊂} + \ldots.$$

While each loop contributes a factor of N, the bare constraint field propagator contributes a factor of $1/N$. We see that the first diagram in the sum above has a factor of $1/N$ associated with it, while the others have a factor of $1/N^2$. We can consider the perturbative expansions in terms of $1/N$ instead of in terms of $\tilde{\lambda}$. This treatment, where we perturb in powers of $1/N$, is called a large-N expansion. This large-N expansion places our perturbation theory on much more solid footing, as we can now actually see whether the parameter we're perturbing in is large or small. For the Heisenberg model, $N = 3$ and so our perturbation parameter is $\frac{1}{3}$, which is not tiny but still relatively small. For the XY model $1/N = \frac{1}{2}$, and for the Ising model $1/N = 1$. We thus see that our perturbative

approach is not useful for the Ising model, and is better suited for the Heisenberg model than for the XY model.

Considering the spin propagator, we get a number of diagrams:

$$K_{\text{eff}\,\vec{q},ij} = \longrightarrow = \longrightarrow + \overset{\frown}{\longrightarrow} + \overset{\frown}{\longrightarrow} + \overset{\frown}{\longrightarrow} + \overset{\frown}{\longrightarrow}$$

$$+ \overset{\frown}{\longrightarrow} + \overset{\frown}{\longrightarrow} + \overset{\frown}{\longrightarrow} + \overset{\frown}{\longrightarrow} + \cdots$$

$$(3.20)$$

Here we have all of the diagrams up to and including $\mathcal{O}(1/N^2)$. We note that the final diagram here is really just the second diagram twice. We can thus define the self-energy $\Sigma_{\vec{q},ij}$ as all of the diagrams of $K_{\text{eff}\,\vec{q},ij}$ with no external legs which are one-particle irreducible, meaning that they cannot be split into two diagrams by cutting a single line. We can equivalently define the polarization $\Pi_{\vec{q},ij}$ as the diagrams in the constraint propagator without external legs which are 1PI. We can thus also define the self-energy and polarization matrices

$$\mathbf{\Sigma}_{\vec{q}\vec{q}',ij} = \Sigma_{\vec{q},ij}\delta_{\vec{q}\vec{q}'}$$

$$\mathbf{\Pi}_{\vec{q}\vec{q}',ij} = \Pi_{\vec{q},ij}\delta_{\vec{q}\vec{q}'}$$

This allows us to write the Dyson equations for the propagators:

$$\longrightarrow = \longrightarrow + \overset{\Sigma}{\longrightarrow}$$

$$(3.21)$$

$$\sim\!\!\sim\!\!\sim = \sim\!\!\sim\!\!\sim + \sim\!\!\overset{\Pi}{\bigcirc}\!\!\sim$$

These equations can be written symbolically as

$$\mathbf{K_{\text{eff}}}^{-1} = \mathbf{K}^{-1} + \mathbf{K}^{-1}\mathbf{\Sigma}\mathbf{K_{\text{eff}}}^{-1} \qquad (3.22)$$

$$\mathbf{D} = \mathbf{D_0} + \mathbf{D_0}\mathbf{\Pi}\mathbf{D} \qquad (3.23)$$

Where $\mathbf{K_{\text{eff}}}_{\vec{q}\vec{q}',ij} = K_{\text{eff}\,\vec{q},ij}\delta_{\vec{q}\vec{q}'}$, $\mathbf{D_0}_{\vec{q}\vec{q}',ij} = D_{0\vec{q},ij}\delta_{\vec{q}\vec{q}'}$ and the products are matrix products in sublattice space. Solving these equations and going back to the $(\vec{q}, ij)$ representation, we get

$$K_{\text{eff}\,\vec{q},ij} = K_{\vec{q},ij} - \Sigma_{\vec{q},ij}$$

$$D_{\vec{q},ij}^{-1} = D_{0\vec{q},ij}^{-1} - \Pi_{\vec{q},ij}. \qquad (3.24)$$

So far, these computations have been exact. To go further, we need to compute Σ and Π in some way. We will do this through the following approximations:

$$\Sigma_{\vec{q},ij} = \overset{\frown}{\longrightarrow} = (-i)^2 \sum_{\vec{p}} D_{\vec{p},ij} K_{\text{eff}\,\vec{q}-\vec{p},ij}$$

$$\Pi_{\vec{q},ij} = \bigcirc - \bigcirc = (-i)^2 \frac{2N}{4} \left[K_{\text{eff}\,\vec{q}+\vec{p},ij}^{-1} K_{\text{eff}\,\vec{p},ji}^{-1} \right] - (-i)^2 \frac{2N}{4} \left[K_{\vec{q}+\vec{p},ij}^{-1} K_{\vec{p},ji}^{-1} \right]$$

Here, we have introduced the two-hook undressed loop. This loop does not actually exist, and we simply use it to cancel out the unphysical part of the two-hook dressed loop. It functions the same way as other loops with j hooks, and carries a factor of $\frac{N}{2}\frac{1}{2}$. The extra factor of 2 is a combinatorial factor.

This self-energy and polarization is only an approximation, as they neglect the vertex correction. We will return to the vertex correction in chapter 5, but first we will show why these expressions for the free energy and polarization are useful. We can now write the Dyson equation for the constraint propagator as

$$D_{\vec{q},ij}^{-1} = D_{0\vec{q},ij}^{-1} - \Pi_{\vec{q},ij} = \frac{N}{2}\left[K_{\vec{q}+\vec{p},ij}^{-1}K_{\vec{p},ji}^{-1}\right] - (-i)^2\frac{N}{2}\left[K_{\mathrm{eff}\,\vec{q}+\vec{p},ij}^{-1}K_{\mathrm{eff}\,\vec{p},ji}^{-1}\right] + (-i)^2\frac{N}{2}\left[K_{\vec{q}+\vec{p},ij}^{-1}K_{\vec{p},ji}^{-1}\right]$$

$$D_{\vec{q},ij}^{-1} = \frac{N}{2}\left[K_{\mathrm{eff}\,\vec{q}+\vec{p},ij}^{-1}K_{\mathrm{eff}\,\vec{p},ji}^{-1}\right]$$

We thus have three relatively simple equations relating the dressed spin propagator, the dressed constraint field propagator, and the self-energy:

$$K_{\mathrm{eff}\,\vec{q},ij} = J_{\vec{q},ij} + \Delta_i\delta_{ij} - \Sigma_{\vec{q},ij}$$

$$D_{\vec{q},ij}^{-1} = \frac{N}{2}\sum_{\vec{p}}K_{\mathrm{eff}\,\vec{p},ij}^{-1}K_{\mathrm{eff}\,\vec{q}-\vec{p},ij}^{-1} \tag{3.25}$$

$$\Sigma_{\vec{q},ij} = -\sum_{\vec{p}}D_{\vec{p},ij}K_{\mathrm{eff}\,\vec{q}-\vec{p},ij}^{-1}$$

3.2   Free energy and saddle point

We have now found a method for expressing the spin propagator diagrammatically. Next, we want to compute the partition function of our model. We have

$$Z = \int D\Delta D\tilde{\lambda}e^{-S[\tilde{\lambda},\Delta]} \tag{3.26}$$

with $S[\tilde{\lambda},\Delta]$ as given in (3.9). If we carry out the Gaussian part of the integral over $\tilde{\lambda}$, we get

$$Z = \int D\Delta e^{-\frac{N}{2}\operatorname{Tr}\ln\mathbf{K}-\frac{1}{2}\operatorname{Tr}\ln\mathbf{D_0}^{-1}+\beta V\sum_i\Delta_i}\int D\tilde{\lambda}e^{\frac{N}{2}\sum_{j\geq 3}\frac{1}{j}\operatorname{Tr}\left(\tilde{\mathbf{\Lambda}}\mathbf{K}^{-1}\right)^j}. \tag{3.27}$$

The second integral contains all of the bubble diagrams contributing to the free energy. We want to capture at least some of these diagrams. We do this by rewriting the action

$$S[\Delta] = \frac{N}{2}\operatorname{Tr}\ln\mathbf{K} + \frac{1}{2}\operatorname{Tr}\ln\mathbf{D_0}^{-1} - \beta V\sum_i\Delta_i - \ln\left(\int D\tilde{\lambda}e^{\sum_{j\geq 3}S_j}\right) \tag{3.28}$$

in terms of the dressed propagators $\mathbf{K}$ and $\mathbf{D}$. We can write

$$\operatorname{Tr}\ln\mathbf{K}_{\mathrm{eff}} = \operatorname{Tr}\ln(\mathbf{K}-\mathbf{\Sigma}) = \operatorname{Tr}\ln\left(\mathbf{K}(\mathbf{1}-\mathbf{K}^{-1}\mathbf{\Sigma})\right) = \operatorname{Tr}\ln\mathbf{K} - \operatorname{Tr}\sum_n\frac{1}{n}(\mathbf{K}^{-1}\mathbf{\Sigma})^n$$

and equivalently for $\mathbf{D}$:

$$\text{Tr} \ln \mathbf{D}^{-1} = \text{Tr} \ln \mathbf{D_0}^{-1} - \text{Tr} \sum_n \frac{1}{n} (\mathbf{D_0} \mathbf{\Pi})^n$$

The action can thus be written as

$$S[\Delta] = \frac{N}{2} \text{Tr} \ln \mathbf{K}_{\text{eff}} + \frac{1}{2} \text{Tr} \ln \mathbf{D}^{-1} - \beta V \sum_i \Delta_i$$

$$+ \frac{N}{2} \text{Tr} \sum_n \frac{1}{n} (\mathbf{K}^{-1} \mathbf{\Sigma})^n + \frac{1}{2} \text{Tr} \sum_n \frac{1}{n} (\mathbf{D_0}^{-1} \mathbf{\Pi})^n - \ln \left(\int D\tilde{\lambda} e^{\sum_{j \geq 3} S_j} \right). \tag{3.29}$$

By using the fact that

$$\text{Tr}(\mathbf{K}_{\text{eff}} \mathbf{\Sigma}) = \sum_n \text{Tr}(\mathbf{K}\mathbf{\Sigma})^n$$

We can rewrite this as

$$S[\Delta] = \frac{N}{2} \text{Tr} \ln \mathbf{K}_{\text{eff}} + \frac{1}{2} \text{Tr} \ln \mathbf{D}^{-1} - \beta V \sum_i \Delta_i + \frac{N}{2} \text{Tr}(\mathbf{K}_{\text{eff}} \mathbf{\Sigma}) + S_r \tag{3.30}$$

with a remainder term

$$S_r = -\frac{N}{2} \text{Tr} \sum_n \frac{n-1}{n} (\mathbf{K}^{-1} \mathbf{\Sigma})^n + \frac{1}{2} \text{Tr} \sum_n \frac{1}{n} (\mathbf{D_0} \mathbf{\Pi})^n - \ln \left(\int D\tilde{\lambda} e^{\sum_{j \geq 3} S_j} \right). \tag{3.31}$$

It is now worth looking at which terms are included in S_r, since all terms not in the remainder must be in the rest of the action. Looking at S_r, we see that the final term, $\ln \left(\int D\tilde{\lambda} e^{\sum_{j \geq 3} S_j} \right)$, contains all closed diagrams. As such, S_r contains all closed diagrams, minus the ones removed by the two first terms of S_r. Looking at the these two terms, we see that they each correspond to a different class of diagrams. The first terms corresponds to spin propagator loops with n self-energy terms on it, while the second corresponds to constraint propagator loops with n polarization terms. In [15], it is shown that these two terms cancel out the corresponding terms in $\ln \left(\int D\tilde{\lambda} e^{\sum_{j \geq 3} S_j} \right)$. Thus, the corresponding diagrams are not in S_r, but rather in the rest of the action.

We approximate the self-energy by excluding S_r from the action. While this removes a lot of diagrams, we hope that the important physics are contained in the loop diagrams which are not in the remainder. We can write this simplified action as

$$S[\Delta] = \frac{N}{2} \text{Tr} \ln \mathbf{K}_{\text{eff}} + \frac{1}{2} \text{Tr} \ln \mathbf{D}^{-1} - \beta V \sum_i \Delta_i + \frac{N}{2} \text{Tr}(\mathbf{K}_{\text{eff}} \mathbf{\Sigma}). \tag{3.32}$$

3.2.1 Saddle point approximation

We now want to carry out the integral with regards to Δ. We do this through the saddle point approximation. In a saddle point approximation, we find the values of Δ which
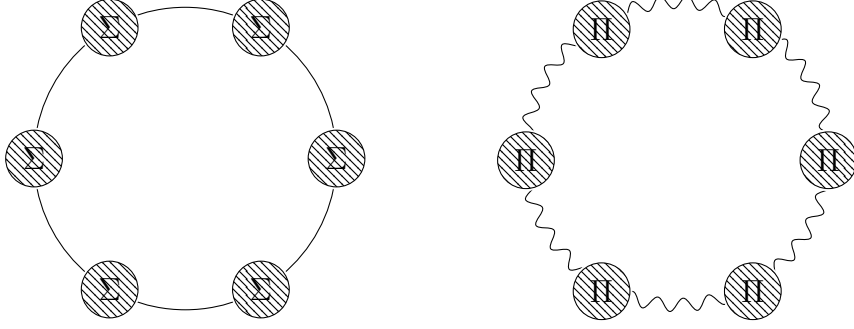
Figure 3.1: Examples of the diagrams which are included in the free energy computation.

extremize the action, which we call Δ_0. We then do a second-order Taylor expansion around this value to capture the most important deviations from the saddle point. This can be written as

$$S[\Delta] \approx S[\Delta_0] + \sum_{ij} \frac{1}{2} \frac{\partial^2 S[\Delta]}{\partial \Delta_i \partial \Delta_j}\Big|_{\Delta=\Delta_0} (\Delta_i - \Delta_{i0})(\Delta_j - \Delta_{j0}). \tag{3.33}$$

Here, Δ is the vector in sublattice space of all the different Δ values on the different sublattices, while Δ_i and Δ_j are the values for specific sublattices. The same applies for Δ_0 and Δ_{i0} & Δ_{j0}, respectively. The saddle point is defined as the point where the derivative of the action is zero:

$$\frac{\partial S[\Delta]}{\partial \Delta_i}\Big|_{\Delta=\Delta_0} = 0 \tag{3.34}$$

We thus calculate the first derivative of the action:

$$\frac{\partial S[\Delta]}{\partial \Delta_i} = \frac{N}{2} \operatorname{Tr}\left(\mathbf{K}_{\text{eff}}^{-1} \frac{\partial \mathbf{K}_{\text{eff}}}{\partial \Delta_i} \right) + \frac{1}{2} \operatorname{Tr}\left(\mathbf{D} \frac{\partial \mathbf{D}^{-1}}{\partial \Delta_i} \right) - \beta V + \frac{N}{2} \operatorname{Tr}\left(\mathbf{K}_{\text{eff}} \frac{\partial \mathbf{\Sigma}}{\partial \Delta_i} + \frac{\partial \mathbf{K}_{\text{eff}}}{\partial \Delta_i} \mathbf{\Sigma} \right) \tag{3.35}$$

We can rewrite this by using the fact that all of these matrices are diagonal in reciprocal space, so we get

$$\begin{aligned}
\frac{\partial S[\Delta]}{\partial \Delta_i} &= \frac{N}{2} \sum_{\vec{q}} \sum_{kl} K_{\text{eff}\,\vec{q},kl}^{-1} \frac{\partial K_{\text{eff}\,\vec{q},lk}}{\partial \Delta_i} + \frac{1}{2} \sum_{\vec{q}} \sum_{kl} D_{\vec{q},kl} \frac{\partial D_{\vec{q},kl}^{-1}}{\partial \Delta_i} - \beta V \\
&\quad + \frac{N}{2} \sum_{\vec{q}} \sum_{kl} \left(K_{\text{eff}\,\vec{q},kl} \frac{\partial \Sigma_{\vec{q},lk}}{\partial \Delta_i} + \frac{\partial K_{\text{eff}\,\vec{q},kl}}{\partial \Delta_i} \Sigma_{\vec{q},lk} \right).
\end{aligned} \tag{3.36}$$

We now consider what some of these derivatives are:

$$\frac{\partial K_{\text{eff}\,\vec{q},kl}}{\partial \Delta_i} = \delta_{ik}\delta_{kl} - \frac{\partial \Sigma_{\vec{q},kl}}{\partial \Delta_i} \tag{3.37}$$

$$\frac{\partial D_{\vec{q},kl}}{\partial \Delta_i} = N \sum_{\vec{p}} K_{\text{eff}\,\vec{q}+\vec{p},kl} \frac{\partial K_{\text{eff}\,\vec{p},lk}}{\partial \Delta_i} \tag{3.38}$$

Thus, we can rewrite the action as

$$\frac{\partial S[\Delta]}{\partial \Delta_i} = \frac{N}{2} \sum_{\vec{q}} K_{\text{eff}\,\vec{q},ii}^{-1} + \frac{N}{2} \sum_{\vec{q}} \sum_{kl} D_{\vec{q},kl} \sum_{\vec{p}} K_{\text{eff}\,\vec{q}+\vec{p},lk} \frac{\partial K_{\text{eff}\,\vec{p},kl}}{\partial \Delta_i} - \beta V$$
$$+ \frac{N}{2} \sum_{\vec{q}} \sum_{kl} \frac{\partial K_{\text{eff}\,\vec{q},kl}}{\partial \Delta_i} \Sigma_{\vec{q},lk} \tag{3.39}$$

We can now use eq. (3.25) for $\Sigma_{\vec{q},ij}$ to further simplify this to

$$\frac{\partial S[\Delta]}{\partial \Delta_i} = -\beta V + \frac{N}{2} \sum_{\vec{q}} K_{\text{eff}\,\vec{q},ii}. \tag{3.40}$$

We thus see that the saddle point requirement is

$$-\beta V + \frac{N}{2} \sum_{\vec{q}} K_{\text{eff}\,\vec{q},ii} = 0. \tag{3.41}$$

We note that this is equivalent to the constraint

$$\sum_{\vec{q}} \langle \vec{S}_{\vec{q},i} \cdot \vec{S}_{-\vec{q},i} \rangle = \sum_{\vec{q}} \frac{NT}{2} K_{\text{eff}\,\vec{q},ii} = V \tag{3.42}$$

which is the constraint imposed by the 0-momentum λ. This is the homogeneous constraint which we related to Δ, so it is natural that this constraint appears here. Indeed, the fact that this constraint appears here shows that our model still maintains this constraint even when considering the approximations that we have made, which in turn suggests that our approximations are good. This also allows us to write the temperature as

$$T_i = \left[\sum_{\vec{q}} \frac{NT}{2V} K_{\text{eff}\,\vec{q},ii} \right]^{-1} \tag{3.43}$$

which will become relevant when doing numerical computations.

We can also compute the second derivative of the action:

$$\frac{\partial^2 S[\Delta]}{\partial \Delta_i \partial \Delta_j} = \frac{\partial}{\Delta_j} \left(-\beta V + \frac{N}{2} \sum_{\vec{q}} K_{\text{eff}\,\vec{q},ii} \right) = -\frac{N}{2} \sum_{\vec{q}} \sum_{kl} K_{\text{eff}\,\vec{q},ik}^{-1} \frac{\partial K_{\text{eff}\,\vec{q},kl}}{\partial \Delta_j} K_{\text{eff}\,\vec{q},li}^{-1} \tag{3.44}$$

which is easily rewritten to

$$\frac{\partial^2 S[\Delta]}{\partial \Delta_i \partial \Delta_j} = -\frac{N}{2} \sum_{\vec{q}} \sum_{kl} K_{\text{eff}\,\vec{q},ik}^{-1} \left(\delta_{jk}\delta_{kl} - \frac{\partial \Sigma_{\vec{q},kl}}{\partial \Delta_j} \right) K_{\text{eff}\,\vec{q},li}^{-1} \tag{3.45}$$

As the diagrams in $\Sigma_{\vec{q},ij}$ are of order $O(1/N)$ or higher, the second derivative to order $\mathcal{O}(N)$ is

$$\frac{\partial^2 S[\Delta]}{\partial \Delta_i \partial \Delta_j} \approx \sum_{\vec{q}} K_{\text{eff}\,\vec{q},ij}^{-1} K_{\text{eff}\,\vec{q},ji}^{-1} = -D_{\vec{q}=0,ij}^{-1} \tag{3.46}$$

Since the action is now quadratic in Δ, we can perform the integral over Δ in the partition function as a Gaussian integral. Performing this integral gives:

$$S = \left(\frac{N}{2} \operatorname{Tr} \ln \mathbf{K}_{\text{eff}} + \frac{1}{2} \operatorname{Tr}_{\vec{q} \neq 0} \ln \mathbf{D}^{-1} - \beta V \sum_i \Delta_i + \frac{N}{2} \operatorname{Tr}(\mathbf{K}_{\text{eff}} \mathbf{\Sigma}) \right) \Big|_{\Delta = \Delta_0} + \frac{1}{2} \ln \mathbf{D}^{-1}_{\vec{q}=0} \tag{3.47}$$

3.2.2 Free energy

Once we have Z, we can compute the free energy density(which we will just refer to as the free energy from now)

$$f = -\frac{1}{\beta V} \ln(Z) \tag{3.48}$$

While we have computed the integral of $e^{-S[\Delta, \tilde{\lambda}]}$, we also need to take into account the several numerical factors that we got during that calculation. We take those factors into account as follows:

Each δ-function which ensured the unit length constraint provides a factor of $\frac{\beta}{\pi}$. The change of variables from λ to Δ and $\tilde{\lambda}$ provides a factor of $V^{Vm/2}$ where m is the number of sublattices. We rescaled each spin by $\frac{1}{\sqrt{\beta}}$ and then performed a Gaussian integral, so each spin component contributes a factor of $\left(\frac{\pi}{\beta} \right)^{1/2}$. Finally, we get a factor of $(2\pi)^{1/2}$ for each Gaussian integral over $\tilde{\lambda}$. Thus, the total constant prefactor is

$$\left(\frac{\beta}{\pi} \right)^{Vm} V^{Vm/2} \left(\frac{\pi}{\beta} \right)^{VNm/2} (2\pi)^{Vm/2}.$$

We can now actually compute the free energy. The constant factors can largely be redistributed into the other terms, so we end up getting

$$f = -\sum_i \Delta_i - \frac{NT}{2V} \sum_{\vec{q}} \operatorname{Tr} \ln \left(T \mathbf{K}_{\text{eff}}^{-1} \right) + \frac{NT}{2V} \sum_{\vec{q}} \operatorname{Tr} \left(\mathbf{K}_{\text{eff}}^{-1} \mathbf{\Sigma} \right) + \frac{T}{2V} \operatorname{Tr} \ln \left(\frac{T^2 \mathbf{D}^{-1}}{2V} \right) - \frac{N-1}{2} \ln(\pi) \tag{3.49}$$

Since all of the matrices are diagonal in $\vec{q}$, we can rewrite this as

$$f = -\sum_i \Delta_i - \frac{NT}{2V} \sum_{\vec{q}} \operatorname{Tr} \ln \left(T K_{\text{eff}\,\vec{q},ij}^{-1} \right) + \frac{NT}{2V} \sum_{\vec{q}} \operatorname{Tr} \left(K_{\text{eff}\,\vec{q},ij}^{-1} \Sigma_{\vec{q},ij} \right) + \frac{T}{2V} \operatorname{Tr} \ln \left(\frac{T^2 D_{\vec{q},ij}^{-1}}{2V} \right) - \frac{N-1}{2} \ln(\pi) \tag{3.50}$$

3.3 Computation

We end up with a set of three self-consistent equations, and a method for computing the temperature:

$$K_{\text{eff}\,\vec{q},ij} = J_{\vec{q},ij} + \Delta_i \delta_{ij} + \Sigma_{\vec{q},ij}$$

$$D_{\vec{q},ij}^{-1} = \frac{N}{2} \sum_{\vec{p}} K_{\text{eff}\,\vec{p},ij}^{-1} K_{\text{eff}\,\vec{q}-\vec{p},ij}^{-1}$$

$$\Sigma_{\vec{q},ij} = \sum_{\vec{p}} D_{\vec{p},ij} K_{\text{eff}\,\vec{q}-\vec{p},ij}^{-1} \tag{3.51}$$

$$T_i = \left(\frac{N}{2V} \sum_{\vec{q}} K_{\text{eff}\,\vec{q},ii}^{-1} \right)^{-1}$$

In these equations, we have flipped the sign of Σ compared to the last sections, as this simplifies some computations. We will keep using this sign-flipped self-energy throughout the rest of this thesis.

Our goal is to solve these equations. To do that, we use an iterative process, where we find $K_{\text{eff}\,\vec{q},ij}$, use that to find $D_{\vec{q},ij}^{-1}$, use that to find $\Sigma_{\vec{q},ij}$ and then use that to find $K_{\text{eff}\,\vec{q},ij}$ again, while checking to see whether the temperature converges as we repeat this process. We will now describe this process in more detail. In addition, an example of a program which performs these calculations is attached as appendix C.

3.3.1 Initializing the process

To start the process, we need some initial guess for Δ_i such that the final temperatures will be the same on all sublattices. We will assume that the temperatures will be the same when all of the Δ's are the same. This usually works for the honeycomb lattice as long as the inter-sublattice coupling is not too small, but it does not work for the kagome lattice. This will be discussed further in chapter 5.

We also need some initial guess for one of the three unknown matrices. We choose to start with a guess for $\Sigma_{\vec{q},ij}$. We will be using random noise to initialize $\Sigma_{\vec{q},ij}$. This random noise needs to be hermitian. To ensure this, we generate some noise $\sigma_{\vec{q},ij}$ with low amplitude and then let $\Sigma_{\vec{q},ij} = \mathcal{F}(\text{Re}(\mathcal{F}^{-1}(\sigma_{\vec{q},ij}))) + h.c$, where $\mathcal{F}$ is the Fourier transformation. When running the code for a range of Δ but the same $J_{\vec{q},ij}$, it can be advantageous to use the $\Sigma_{\vec{q},ij}$ found in one run as the initial guess for the next run. When doing this, it is important to include some symmetry-breaking noise when initializing the next run.

3.3.2 Iterative calculation

Now that the process has been initialized, we can perform the iterations. We iteratre using the following procedure:

1. Subtract the minimum eigenvalue of $J_{\vec{q},ij} + \Sigma_{\vec{q},ij}$ from $\Sigma_{\vec{q},ij}$

2. Calculate $K_{\text{eff}\,\vec{q},ij}$ and invert it

3. Calculate T_i. If T_i is close to $T_{i,old}$, stop the loop

4. Calculate $D_{\vec{q},ij}^{-1}$ and invert. Set $D_{\vec{q}=0} = 0$

5. Calculate $\Sigma_{\vec{q},ij}$

6. Go to step 1

Once the loop has stopped, we check whether all of the T_i are equal. If they are, we can proceed to compute various observable quantities from $K_{\text{eff}\,\vec{q},ij}^{-1}$, $\Sigma_{\vec{q},ij}$ and $D_{\vec{q},ij}$. The results from our self-consistent equations are only valid if all T_i are equal.

One problem with NBT in 2d is that it will sometimes converge on states which break inversion symmetry, which is not allowed by the Mermin-Wagner theorem, as broken inversion symmetry is equal to a broken spin-rotation symmetry. This seems to be either a finite-size effect or a numerical artifact. To avoid this, we manually set $\Sigma_{\vec{q},ij}$ to be inversion symmetric.

3.3.3 Subtracting eigenvalues

As the first step in the convergence loop, we subtract the minimal eigenvalue of $J_{\vec{q},ij} + \Sigma_{\vec{q},ij}$ from the diagonal of $\Sigma_{\vec{q},ij}$. Labeling this minimal value as Σ_{min}, we can see that this is permitted by rewriting what we are doing as

$$K_{\text{eff}\,\vec{q},ij} = J_{\vec{q},ij} + \Delta_i \delta_{ij} + (\Sigma_{\vec{q},ij} - \Sigma_{min}\delta_{ij}) = J_{\vec{q},ij} + (\Delta_i - \Sigma_{min})\delta_{ij} + \Sigma_{\vec{q},ij}.$$

We see what we are doing is actually just redefining $\Delta_i \to \Delta_i - \Sigma_{min}$, and since Δ_i is an arbitrary real parameter, this is allowed. It is however important to keep this in mind when computing the free energy, as that requires that we use this "renormalized" Δ_i. This step ensures that the minimal eigenvalue of $K_{\text{eff}\,\vec{q},ij}$ is Δ. This seems to be the reason why this step is important, as the solutions to the self-consistent equations are dependent on this minimum eigenvalue of $K_{\text{eff}\,\vec{q},ij}$. If this step is performed incorrectly, the equations will converge to a temperature determined by the smallest eigenvalue of $K_{\text{eff}\,\vec{q},ij}$. As this is almost always at least as large as Δ, this means that the equations will converge to a higher-temperature state, and low-temperature states may not be reachable.

It is worth noting that the renormalization described here is different than that described

in [2,15]. In these works, they normalize $J_{\vec{q},ij}$ such that its minimal eigenvalue is zero, and then let Σ_{min} be the minimal eigenvalue of $\Sigma_{\vec{q},ij}$. This approach also works most of the time, but can lead to problems when analyzing spiral states, especially for non-Bravais lattices. In these cases, the minimal value of $J_{\vec{q},ij}$ and $\Sigma_{\vec{q},ij}$ does not necessarily happen at the same $\vec{q}$, and as such minimizing both independently does not necessarily minimize their sum. Defining Σ_{min} as the minimal eigenvalue of $\Sigma_{\vec{q},ij} + J_{\vec{q},ij}$ is more consistent in these cases. This also means that it is not necessary to normalize $J_{\vec{q},ij}$ such that its minimal eigenvalue is zero, but we still choose to do so as it is still the most natural choice of normalization.

3.3.4 Convolution

The key reason why Nematic Bond Theory is a worthwhile approach to analyzing magnetic systems is that it is much faster than other computational methods like Monte Carlo. The reason for this increased speed lies in the computation of the sums in (3.51). Here, we can use the convolution theorem.

The convolution theorem states that

$$\mathcal{F}(f * g) = \mathcal{F}(f) \cdot \mathcal{F}(g) \tag{3.52}$$

where $*$ denotes the convolution of two functions. The convolution can be written as:

$$(f * g)(t) = \int d\tau f(\tau) g(t - \tau)$$

Noting that the sums in (3.51) are the discrete version of this convolution, we thus see that we can write them as Fourier transforms:

$$D_{\vec{q},ij}^{-1} = \mathcal{F}(\mathcal{F}^{-1}(K_{\text{eff}\,\vec{q},ij}) \cdot \mathcal{F}^{-1}(K_{\text{eff}\,\vec{q},ij})) \tag{3.53}$$

Where we use the fact that the Fourier transform and its inverse have similar forms. Physically, this means that we compute these sums in reciprocal space by going to real space, where they are simply products. Using the fast Fourier transform algorithm, we can do this in $O(N \log N)$ time, where N is the number of lattice sites. Meanwhile, if we were to simply perform the sums, that would take $O(N^2)$. In addition, Monte Carlo is also $O(N^2)$, and as such Nematic Bond Theory scales significantly more efficiently for large inputs. This alone does not guarantee that the model is computationally viable, but it is reasonably easy to implement the model in a way that is significantly faster than Monte Carlo, even for relatively small systems.

3.3.5 Convergence

Each time we iterate eqs. (3.51), we need to check whether they have converged on a solution. To do this, we compare the temperature T to the temperature found in the

previous iteration T_{old}. Specifically, we say that the equations have converged if

$$\frac{|T - T_{old}|}{T_{old}} < 10^{-8}.$$

The exact value of the right-hand side is not important to the computation, as long as it is small.

To ensure that the program actually halts at some point, we only allow it to run for 200 iterations. Usually, this is more than enough to ensure convergence, but around the critical point the system may converge very slowly or not at all. The non-converging states are often metastable states, and as such are not particularly important for the computation of observable properties of the model.

3.3.6 Free energy and heat capacity

We found that the free energy is given by (3.50). However, this expression does not include the renormalization of Δ or the sign change of Σ. When we include this, we get

$$f = -(\Delta - \Sigma_{min}) - \frac{NT}{2V}\sum_{\vec{q}}\ln TK_{eff\vec{q}}^{-1} - \frac{NT}{2V}\sum_{\vec{q}}\Sigma_{\vec{q}}K_{eff\vec{q}}^{-1} + \frac{T}{2V}\sum_{\vec{q}}\ln\left(\frac{T^2 D_{\vec{q}}^{-1}}{2V}\right) - \frac{N-1}{2}T\ln(\pi)$$

(3.54)

Here, it is important to remember that the sum in the fourth term also includes $\vec{q} = 0$. While including this term does not have a large effect in practice, it is still important to ensure the correctness of the implementation of NBT.

When doing NBT calculations, it is possible that different Δ will lead to the same T. In this case, the different Δ lead to different phases at the same temperature. This means that the two different Δ which lead to the same T lead to different free energies, and as such we can distinguish between the thermal state, which is the state with the lowest free energy, and the metastable state(s) which have a higher energy. Usually, the metastable states and the thermal state have different symmetry properties, with one state being the high-symmetry state and another being the low symmetry. In theory, we could compute the free energy for the high-symmetry state and low-symmetry state for all T, and we can recognize the place where these free energies cross as the phase transition. In practice, Nematic Bond Theory only gives multiple states for the same T in regions where the energy difference between the thermal state and the metastable state is small. In other words, this primarily happens near a phase transition. The presence of metastable states hints that we are working with a first-order phase transition. This is not guaranteed, however. The presence of metastable states can be due to finite-size effects. In that case, we would expect the metastable states to disappear as we increase the system size, and thus it is possible to distinguish between first-order and second-order transitions. This has been done with NBT a number of times [2, 17], but we will not be considering it in

this thesis.

In practice, we only compute f for a discrete number of Δ, and the crossing might very well lie for Δ's in between. We thus find the critical temperature by linearly interpolating between the computed values of f and finding the place where the two branches of f cross. Another key use of the free energy is computing the specific heat of the system, which can be written as

$$c_v = -T\frac{\partial^2 f}{\partial T^2}$$

Here, however, we run into a few complications. The first complication is the fact that we only know the free energy at a discrete number of points. As these points are not evenly spaced, we need to be careful when taking the second derivative. When computing the specific heat at a temperature T_i with associated free energy f_i, we do this by computing the quadratic that goes through $(T_{i-1}, f_{i-1}), (T_i, f_i)$ and (T_{i+1}, f_{i+1}), and then multiplying the second derivative of this quadratic by $-T_i$.

This approach works as long as there are no phase transitions. When we have phase transitions and thus a multivalued free energy, we also get a multivalued specific heat. To avoid this, we only consider the lowest branch of the free energy. This leads to a spike in the free energy at the phase transition. The height of this spike depends on the exact points where the temperature and free energy are computed, and the theoretically "correct" height of the spike is infinite.

3.3.7 Structure factor

An important observable is the structure factor. The structure factor is what is observed by a neutron scattering experiment, and as such it is a primary way to measure magnetic order.

The structure factor is simply proportional to the susceptibility. To compute it, we need to take into account the different positions of the sublattices, as the neutron scattering cannot tell the difference between magnetic moments on different sublattices. We can write the structure factor as

$$\mathcal{S}(\vec{q}) = \frac{NT}{2}\sum_{ij} K_{\text{eff}\,\vec{q},ij}e^{-i\vec{q}\cdot\vec{\alpha}_{ij}} \tag{3.55}$$

where α_{ij} is the displacement vector between sublattices i and j.

Chapter 4

Results

4.1 The honeycomb lattice

The honeycomb lattice is the lattice formed by tiling the plane with regular hexagons. In this way, it is similar to the square and triangular lattices. Unlike these, however, it is not a Bravais lattice. As such, the honeycomb lattice is a natural stepping stone between the relatively simple square and triangular lattices and complex lattices like the kagome lattice, which shows large degrees of geometric frustration.

The honeycomb lattice can be defined as two triangular lattices, each with lattice vectors

$$\vec{a}_1 = \begin{pmatrix} 1 \\ 0 \end{pmatrix}, \vec{a}_2 = \begin{pmatrix} \frac{1}{2} \\ \frac{\sqrt{3}}{2} \end{pmatrix}. \tag{4.1}$$

These two triangular lattices are related by the vector

$$\vec{\alpha} = \begin{pmatrix} 0 \\ \frac{\sqrt{3}}{3} \end{pmatrix}. \tag{4.2}$$

From the definition of the honeycomb lattice, we can fairly easily see that it is bipartite, meaning that it can be divided into two sections such that for each atom in one section, all of its nearest neighbors are in another section. For the honeycomb lattice, these two sections are simply the two sublattices. The honeycomb lattice shares this feature with the square lattice, but not with the triangular lattice.

The fact that the lattice is bipartite means that the frustration of the lattice cannot come from geometry alone, but must come from longer-range couplings. Specifically, we are going to analyze first, second and third-nearest neighbor couplings with the coupling strengths J_1, J_2 and J_3 respectively. In the language of NBT, these interactions are represented by a 2×2 matrix $J_{\vec{q},ij}$. Introducing $\vec{a}_3 = \vec{a}_2 - \vec{a}_1$, we can write

$$J_{\vec{q}} = \begin{pmatrix} J_{\vec{q},11} & J_{\vec{q},12} \\ J_{\vec{q},21} & J_{\vec{q},22} \end{pmatrix} \tag{4.3}$$

where

$$J_{\vec{q},11} = J_2 \cdot \left(\cos(\vec{a}_1 \cdot \vec{q}) + \cos(\vec{a}_2 \cdot \vec{q}) + \cos(\vec{a}_3 \cdot \vec{q}) \right),$$

$$J_{\vec{q},12} = \frac{1}{2} \left(J_1 \left(1 + e^{-i\vec{q}\cdot\vec{a}_2} + e^{-i\vec{q}\cdot\vec{a}_3} \right) + J_3 \left(e^{i\vec{q}\cdot\vec{a}_1} + e^{-i\vec{q}\cdot\vec{a}_1} + e^{-i\vec{q}\cdot(\vec{a}_2+\vec{a}_3)} \right) \right),$$

$$J_{\vec{q},21} = J_{\vec{q},12}^*,$$

$$J_{\vec{q},22} = J_{\vec{q},11}$$

(4.4)
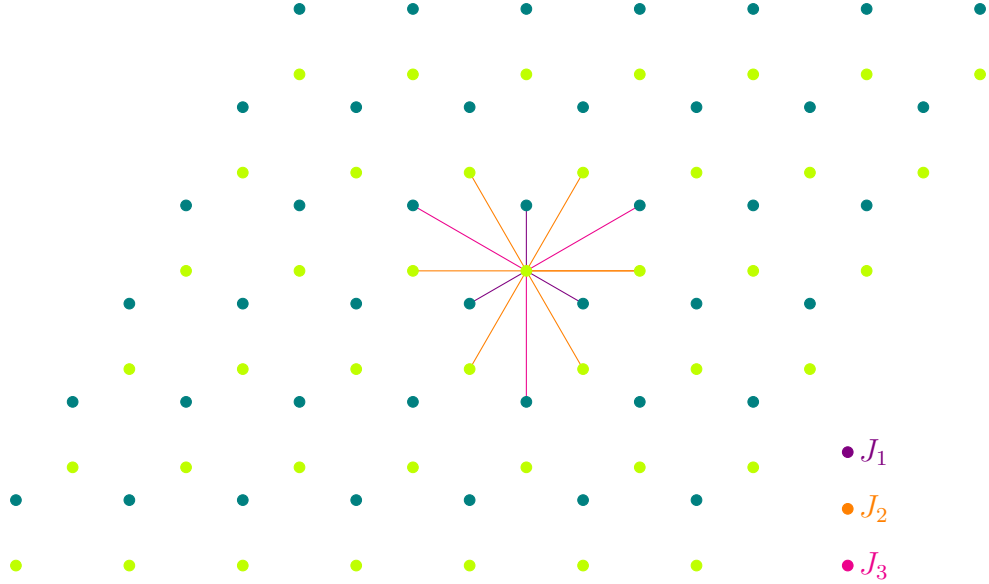
Figure 4.1: Honeycomb lattice with J_1-J_2-J_3. The two sublattices have two different colors.

We note that the first- and third-nearest neighbor couplings are between different sublattices, while second-nearest neighbor couplings is within the same sublattice. This means that the hamiltonian is invariant under the action of mapping all the spins of one sublattice from $\vec{S}$ to $-\vec{S}$ and mapping $J_1 \to -J_1$, $J_2 \to J_2$, $J_3 \to -J_3$. From the standpoint of thermodynamics, this sign flip doesn't matter, and as such we can choose to let $J_1 = 1$ for all of our computations, and thus measure the strength of the other couplings in units of J_1.

Honeycomb lattices with third-nearest neighbor couplings are found in a number of materials, including NiS_2 [7] and the family of materials XPS_3 with $X = Ni, Co, Fe$ [18–20]. In all of these materials, the third-nearest neighbor coupling is the dominant one. The nickel compound is particularly interesting for our purposes as the anisotropy is relatively small, and as such it is well-described by the Heisenberg hamiltonian.

4.1.1 Zero-temperature phase diagram

The zero-temperature phase diagram of the hexagonal lattice with J_1, J_2 and J_3 coupling was reported in [21]. Here, two different phase diagrams are reported, for both ferro-

magnetic and antiferromagnetic J_1. Each of these phase diagrams contain six different phases:

- A ferromagnetic phase, where all of the spins are pointed the same way.

- An antiferromagnetic phase, where the spins on the two different sublattices are pointed different ways.

- A stripe phase, where the spins are aligned in one direction and antialigned in another direction.

- A dimer phase, where two nearest-neighbor spins form a pair which is aligned, and is then antialigned with neighboring pairs.

- Two different incommensurate spiral phases, which we label III and V in accordance with [21].
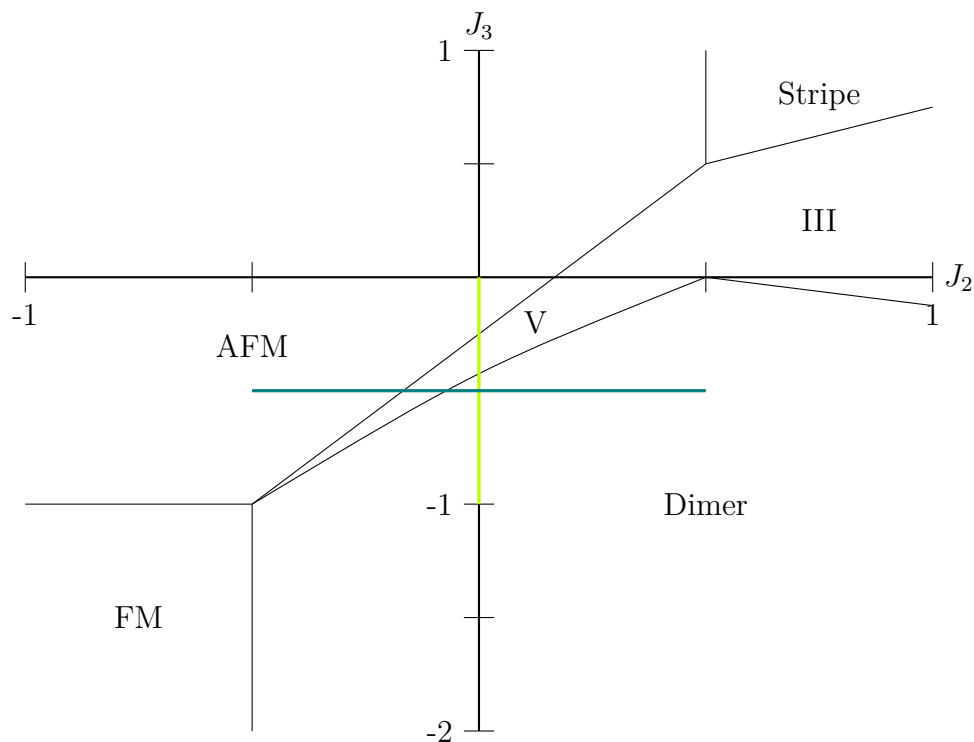
Figure 4.2: Zero-temperature phase diagram for the J_1-J_2-J_3 honeycomb lattice, as described in [21]. The blue and green lines are the lines where we will compute the critical temperature.

32

(a) Stripe phase   (b) Dimer phase
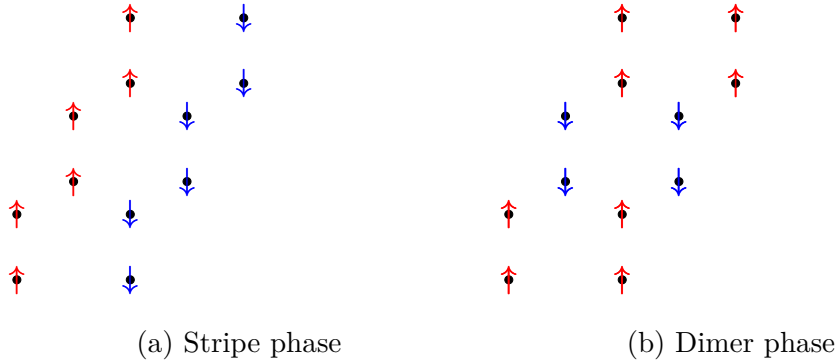
Figure 4.3: Examples of the stripe phase and dimer phase of the honeycomb lattice.

The mapping described in section 4.1 maps between the ferromagnetic and antiferromagnetic phases, and between stripe and dimer phases. It maps each of the incommensurate spiral phases to themselves.

Each of these phases have different structure factors, as described in [22]. The ferromagnetic phase has a maximal structure factor at the Γ point, the antiferromagnetic at the K point, the dimer phase at the M point of the reduced Brillouin zone, and the stripe phase at the M point of the extended Brillouin zone. The incommensurate phases can also be distinguished by their structure factors. For the phase V in [21], the maximum of the structure factor lies on the Brillouin zone boundary, whereas for phase III it lies inside the Brillouin zone. Thus, we can characterize what phase we're in by looking at the structure factor.

A large section of the $J_1 - J_2 - J_3$ phase diagram can host nematic transition. We can analyze these phase transition by defining an order parameter [23]

$$O_{12} = \frac{1}{2V}\langle \vec{S}_{\vec{q},1} \cdot \vec{S}_{\vec{q},2}\rangle \left(1 + e^{2\pi i/3}e^{i\vec{q}\cdot\vec{a}_1} + e^{4\pi i/3}e^{i\vec{q}\cdot\vec{a}_2}\right) \tag{4.5}$$

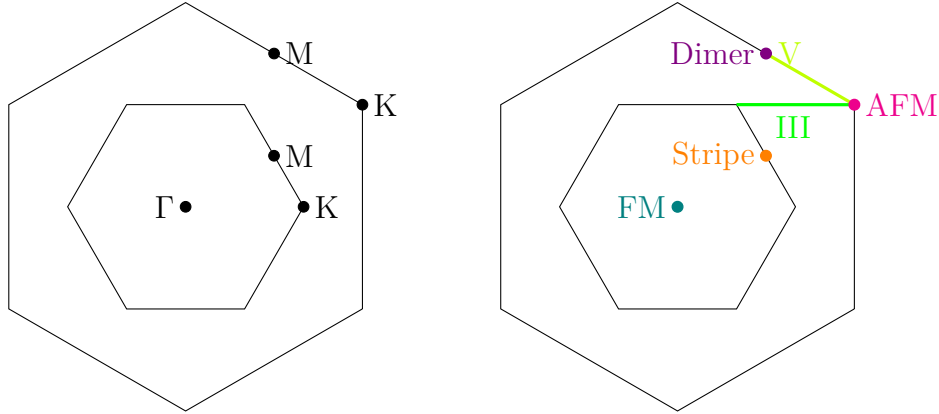which shows whether the correlations between sublattices are stronger in one direction than in other.

Figure 4.4: On the left, the Brillouin zone for the honeycomb lattice with various symmetry points labelled. Note that the labels M and K can both refer to points on the inner and outer hexagon, referred to as the reduced and extended Brillouin zones respectively [22]. On the right, the maximum of the structure factor for the various phases of the honeycomb model. For phases III and V, the maximum lies on the respective colored lines.

We can use Nematic Bond Theory to compute the transition temperature and structure factor for various values of J_1-J_2-J_3. We do the computation on a 200×200 grid, which means a total of 80000 lattice points. We choose to use J_1 as our unit of energy and temperature, and the distance between unit cells a as our unit of length. When computing the free energy, order parameter and T_c, we do the NBT calculations for 50 Δ's chosen on a logarithmic scale between 1 and 10^{-8}.

4.1.2 Nematic transition on the honeycomb lattice

We can start by considering a single point in parameter space: $J_3 = -0.5$, with $J_2 = 0$. This point lies in the dimer phase, meaning that there are three distinct ordering vector: One for each M point in the extended Brillouin zone which is unique under inversion symmetry. Looking at the free energy, we see that it is multivalued around $T = 0.29$. This multivaluedness is a sign of the presense of metastable states, which in turn is a sign of a first-order phase transition. We can thus see that there is a phase transition, with $T_c \approx 0.29$.
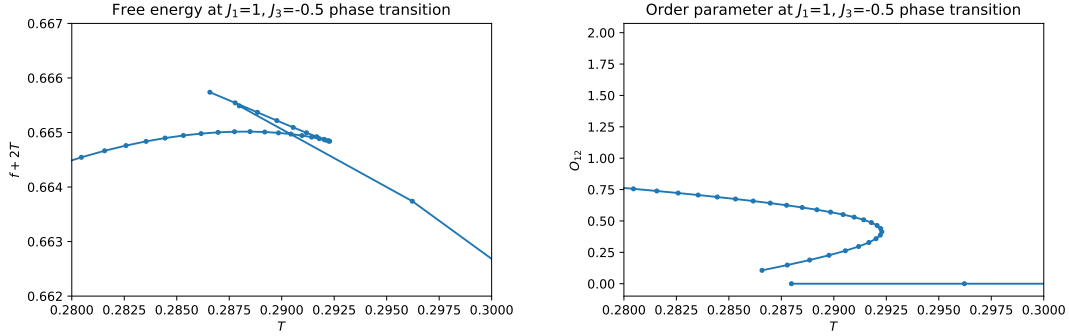
Figure 4.5: The free energy and order parameter for the $J_3 = -0.5$ honeycomb lattice at the phase transition. The free energy is scaled to make the discontinuity more clear. In both cases, the lines connecting the points is cut in two, representing the fact that between these two states there are one or more non-converging states.
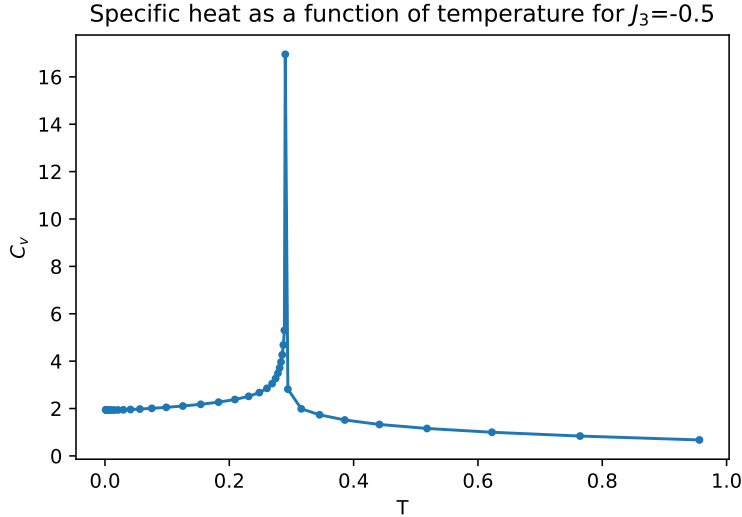

Figure 4.6: Heat capacity for the $J_3 = -0.5$ honeycomb lattice. The heat capacity diverges at T_c, so the height of the peak is not a useful measure.

We can also compute the order parameter at various temperatures. Doing this, we note that the order parameter is multivalued in the region where the free energy is multivalued. We also note that for high temperatures, the order parameter is zero, while for low temperatures it is non-zero. This confirms that a phase transition does take place, and that this phase transition is related to the breaking of the Z_3 symmetry of the lattice. From the free energy, we can compute the specific heat. Doing this, we see that it diverges at T_c, exactly as we would expect from a first-order phase transition. We note that for $T \to 0$, the specific heat goes to 2. This might seem surprising, as both experiment and spin wave theory suggest that in magnetic materials, the specific heat should go to zero for low temperatures. In addition, this is also a requirement of the third law of

thermodynamics. The fact that it goes to 2 is a property of the classical $O(N)$ model which will be explored further in chapter 5.

Looking at the structure factor above and below T_c, the phase transition is easily identifiable. Above T_c, we see that the structure factor has a maxima at each of the ordering vectors,and thus has sixfold symmetry, while below T_c it only has maxima at one of the ordering vectors and thus only maintains inversion symmetry. We also observe that above the critical temperature, the peaks in the structure factor are much broader. This indicates that the fluctuations around the ordering vectors are larger. At these temperatures, there is also a significant structure factor away from the $\vec{Q}$-vectors.
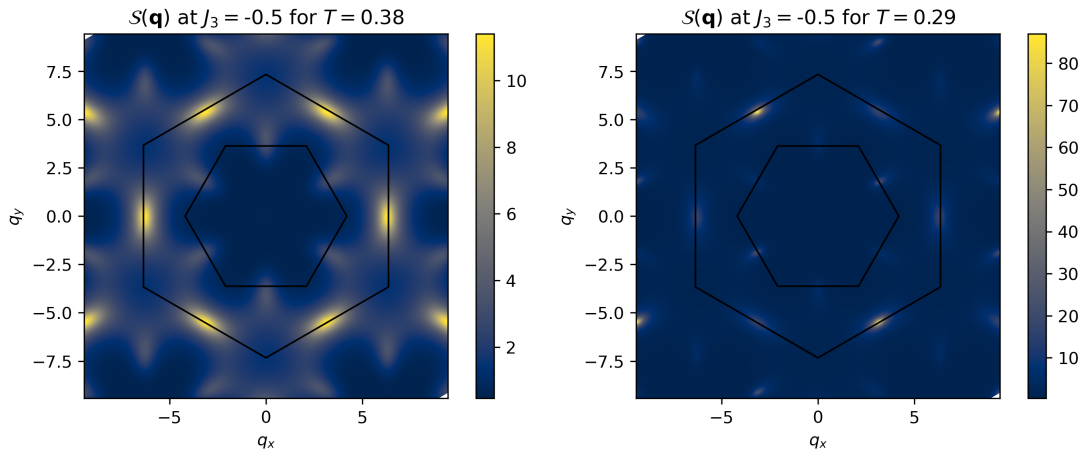

Figure 4.7: The structure factor at $T = 0.38$ and $T = 0.29$ for the $J_3 = -0.5$ honeycomb lattice. The high-T phase has sixfold symmetry, while the low-T phase only has twofold symmetry.

J_1-J_3 phase diagram

Now that we know what a phase transition looks like, we can consider the transition temperature along the line $J_2 = 0$ with $J_3 < 0$. We see that a phase transition begins around $J_3 = -0.25$. Here, we go from an antiferromagnetic ground state to an incommensurate spiral, and then to a dimer ground state as J_3 is decreased further. The phase transition temperature increases continuously as $|J_3|$ increases. We see that for large $|J_3|$, the transition temperature is proportional to J_3, but for smaller $|J_3|$ the transition temperature is smaller than this proportionality would predict. This is seen in other frustrated systems like the square-lattice $J_1 - J_2$ model [24]. The proportionality at large $|J_3|$ is explained by the fact that for a magnetic system with one dominant interaction, we have $T_c \propto J$. For smaller $|J_3|$, the competing interactions mean that this no longer holds.
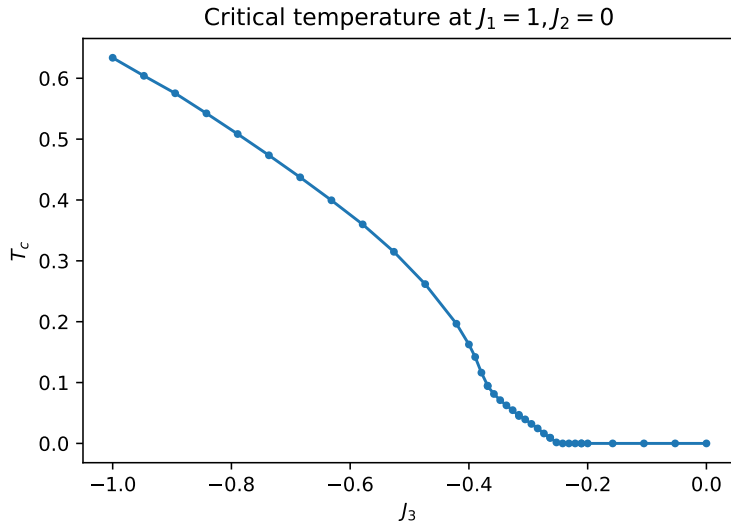
Figure 4.8: Nematic transition temperature as a function of J_3.

The behavior around the phase transition is different from that found in Weber et al. [24] for the $J_1 - J_2$ square lattice. They find that at the parameters where the phase transition sets in, the critical temperature is not smooth, but is continuous. Meanwhile, we find that the critical temperature smoothly goes from zero to a finite temperature as we vary the relevant parameter. It is unclear whether this is due to the fact that the phase transition initially happens in a spiral regime in the honeycomb model, while for the square model it happens in a collinear regime. However, the results from [12] suggest that the critical temperature is also non-smooth for transitions to a spiral state in the honeycomb model with $J_3 = 0$. What our results suggest is that the non-smooth change in transition temperature is not a universal feature of frustrated magnets.
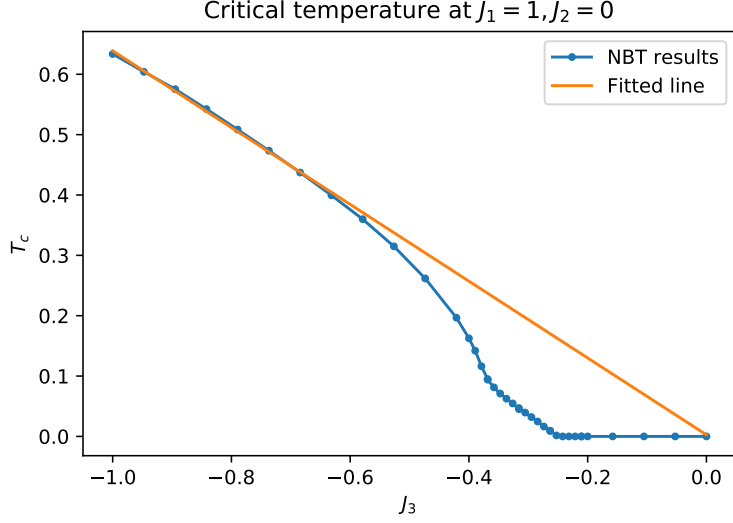
Figure 4.9: Nematic transition temperature as a function of J_3, with a linear relationship fitted to the range $J_3 > -0.7$.

J_1-J_2-J_3 model

We now consider adding in a non-zero intra-sublattice coupling J_2. As the case where $J_3 = 0$ has been thoroughly studied by NBT [15], we will not focus on that. Instead, we will consider the case where $J_3 = -0.5$. Here, we already have a nematic transition when $J_2 = 0$. We see that for positive J_2, the transition temperature is increased, while for negative J_2 it is decreased. When J_2 is negative enough, it pushes the system into an antiferromagnetic region where there is no nematic transition. Here, we also observe that the critical temperature changes smoothly from zero as we enter the region that can host a nematic transition. As the $J_2 = 0$ case already has a nematic transition, we do not expect to see $T_c \propto J_2$ behavior.
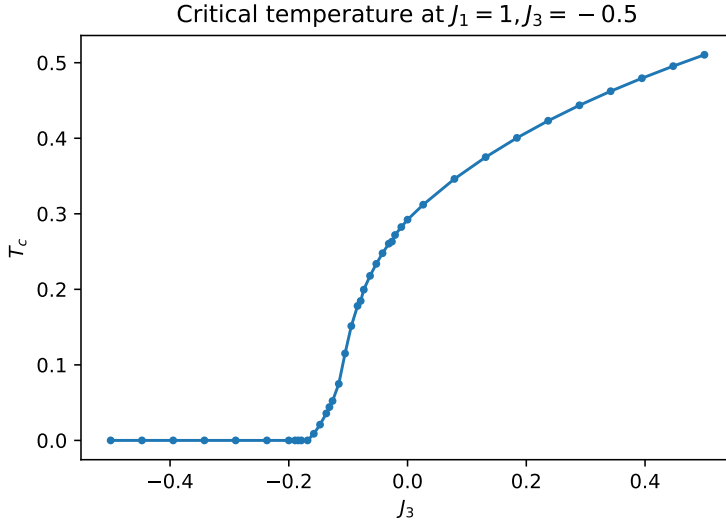
Figure 4.10: Nematic transition temperature as a function of J_2 for $J_3 = -0.5$

Maximally frustrated point

We consider the maximally frustrated point as considered in [25], where $J_2 = J_3 = \frac{J_1}{2}$. At this point, the ground state manifold consists of all states where the sum of spins on each hexagon $\vec{S}_{\hexagon} = 0$. This phase, known as the Coulomb phase, shows macroscopic ground state degeneracy, and the structure factor is characterized by pinch points, as described in [11]. This is also what [25] observed with Monte Carlo simulation of a 1800-spin system. When we compute the structure factor using NBT, we observe the pinch points as well. In addition, we can check that these pinch points are there at a large range of temperatures, and that there is no phase transition. All of this is consistent with the description of a Coulomb phase. Thus, this indicates that NBT does work on the honeycomb lattice with $J_1 - J_2 - J_3$, even in the highly frustrated regimes. This indicates that NBT captures the physics of highly frustrated non-Bravais lattices.
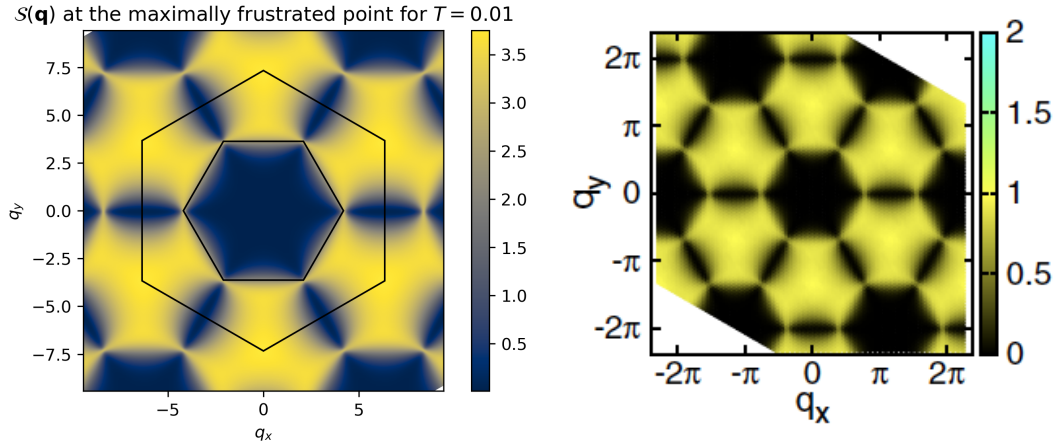
Figure 4.11: NBT computation of the structure factor at the maximally frustrated point, compared with Monte Carlo calculations, both at $T \approx 0.01$. Monte Carlo calculations from [25]. The different scales are due to different normalizations of the spins.

4.2 RKKY crystal

The RKKY interaction is an interaction between two localized spins mediated by a sea of conduction electrons. Specifically, the interaction is caused by one spin polarizing the conduction electrons, and the other spin then interacting with the now polarized electrons, leading to an effective spin-spin interaction. The details of the interaction depends on the Fermi surface of the material, but in the simplest case of a spherical Fermi surface in a 3d material, the interaction has the form

$$J(r_{ij}) = J\left(\frac{\cos(2k_F r_{ij})}{(2k_F r_{ij})^3} - \frac{\sin(2k_F r_{ij})}{(2k_F r_{ij})^4}\right). \tag{4.6}$$

This model has two parameters: J and k_F. J is the coupling strength of the RKKY coupling, and can be factored out by measuring all energies and temperatures in units of J, similarly to what we do for the exchange coupling. Thus, the only parameter that can actually affect the behavior of this model is k_F, the length of the Fermi vector for the electrons. For our purposes, k_F is simply a parameter of the model which we can vary freely.

We consider an RKKY crystal: A lattice of spins interacting through the RKKY interaction. In particular, we consider a triangular lattice. This lattice can be described by the lattice vectors given in (4.1). Physically, this model can be realized in several different ways. One realization is through the deposition of magnetic adatoms on a conductive surface. In this realization k_F, when measured in units of the reciprocal lattice constant of the adatoms, depends on the spacing of the adatoms. In addition, there are materials where the RKKY interaction is the dominant interaction between spins, for example Gd_2PdSi_3 [5, 26–28].

The $1/r^n$ decay of this interaction makes it interesting in that it is very different from the exchange interaction, but it also poses some challenges. In particular, when considering a system with periodic boundary conditions, the interaction happens not just between spins within one period of the lattice, but also between spins in different periods. Computing the full potential then involves the infinite sum [29]

$$J_{ij} = J \sum_{\vec{\lambda}} \left(\frac{\cos\left(2k_F(r_{ij} + \vec{\lambda})\right)}{(2k_F(r_{ij} + \vec{\lambda}))^3} - \frac{\sin\left(2k_F(r_{ij} + \vec{\lambda})\right)}{(2k_F(r_{ij} + \vec{\lambda}))^4} \right)$$

where $\vec{\lambda}$ are the vectors connecting the different periods of the system. They can be written as

$$\vec{\lambda} = m\vec{a}_1 L + n\vec{a}_2 L, \quad m, n \in \mathbb{Z} \tag{4.7}$$

where L is the length of the system. Evaluating this sum is difficult due to the fact that it converges fairly slowly. In [29], the Ewald sum method is used to evaluate the sum. This method works by dividing the sum into a short-range and a long-range part, and then computing the long-range part in reciprocal space. For the RKKY interaction in 2d, this leads to an integral for each lattice site. These integrals must be computed numerically, which is computationally expensive, and as such this method is not feasible for large lattices. Instead, we simply perform the sum in real space, relying on the fact that on a large lattice the non-leading terms of the sum should be tiny. To check our method, we can compare the zero-temperature phase diagram that we find with the diagram found by [29] using the Ewald method on a significantly smaller lattice. We see that the zero-temperature phase diagrams are the same. We also see that including $\vec{\lambda}$ beyond the leading-order terms of $(0, 0), (0, 1), (1, 0)$ and $(1, 1)$ has a negligible effect on the potential.
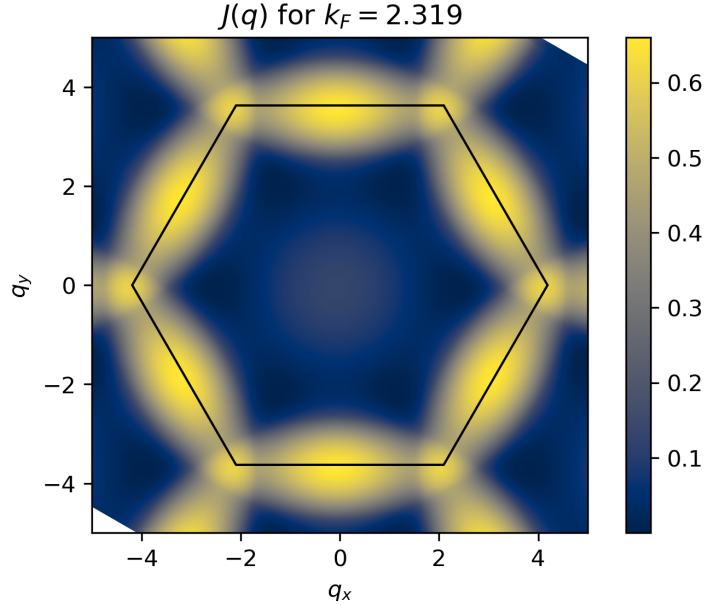
Figure 4.12: $J(\vec{q})$ for $k_F = \frac{2\pi}{2.71}$. The black hexagon marks the first Brillouin zone.

To analyze nematic transitions on the triangular lattice, we can define an order parameter

$$I = \frac{1}{2V} \sum_{\vec{q}} \langle \vec{S}_{\vec{q}} \cdot \vec{S}_{-\vec{q}} \rangle (e^{i\vec{q}\cdot\vec{a}_1} + \omega e^{i\vec{q}\cdot\vec{a}_2} + \omega^2 e^{i\vec{q}\cdot(\vec{a}_2 - \vec{a}_1)})$$ (4.8)

where $\omega = e^{2\pi i/3}$ is a third root of unity. This order parameter is zero when the Z_3 symmetry of the lattice is present, and is non-zero when that symmetry is broken. We will be considering the absolute value of this order parameter.

4.2.1 Zero-temperature phase diagram

From the point of view of NBT, the most interesting region of parameter space is $2.11 < k_F < 2.44$, as this is region has an incommensurate spiral ground state which can show nematic order. Above $k_F = 2.44$, the system has a ferromagnetic ground state, while below $k_F = 2.11$ it is in the 120° state, with the $\vec{Q}$-vector lying on the K point of the Brillouin zone. In the region in between, the $\vec{Q}$-vector lies on the line connecting the Γ point to the K point. By computing $\left|\vec{Q}\right|$ at various k_F, we see that the ordering vector changes continuously as we move in parameter space.
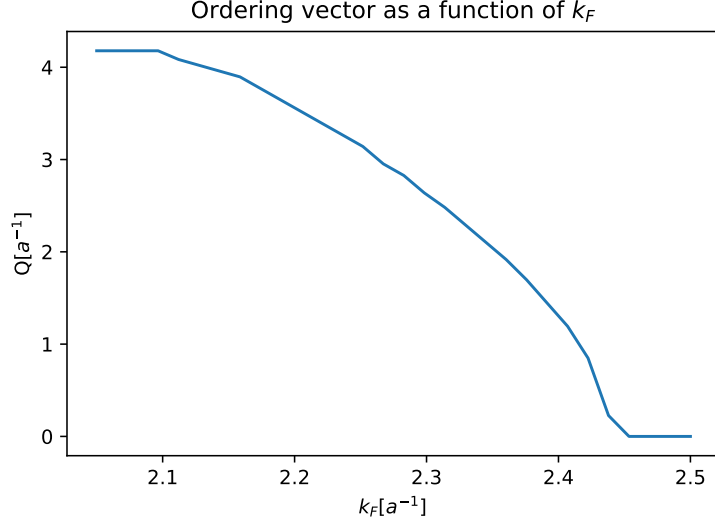
Figure 4.13: $\left|\vec{Q}\right|$ as a function of k_F for k_F between 2 and 2.5. For $\frac{4\pi}{3} > \left|\vec{Q}\right| > 0$, we are in a nematic phase.

The fact that $\vec{Q}$ changes continuously makes this region different from another region of parameter space: between $k_F = 3.67$ and $k_F = 2.85$, we also observe a spiral ground state. In this region, the ordering vector changes discontinuously at $k_F = 3.85$ from somewhere inside the Brillouin zone to the K point, which corresponds to 120° ordering. We will primarily look at the region $2.11 < k_F < 2.44$, as it is the one where [29] has performed their studies of the presence of skyrmions when an external magnetic field is applied.
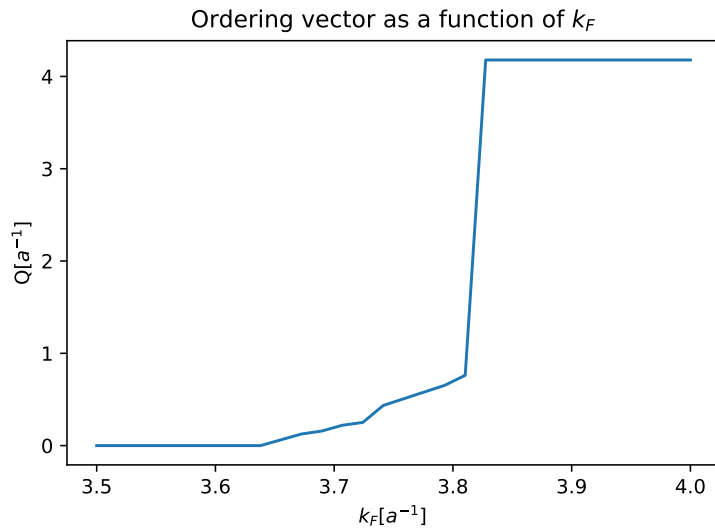

Figure 4.14: $\left|\vec{Q}\right|$ as a function of k_F for k_F between 3.5 and 4. We see that the ordering vector changes discontinuously in this range.

Looking at $J_{\vec{q}}$ for a number of different k_F, we see that near the 120°-nematic transition point, $J_{\vec{q}}$ is relatively large on the Brillouin zone boundary, as well as at the Γ point. As we move into the nematic region, the large value at the Brillouin zone boundary is maintained, but the value at the Γ point lowers considerable, and near the nematic-ferromagnetic boundary there is a large region of reciprocal space around the Γ where $J_{\vec{q}}$ is very small.
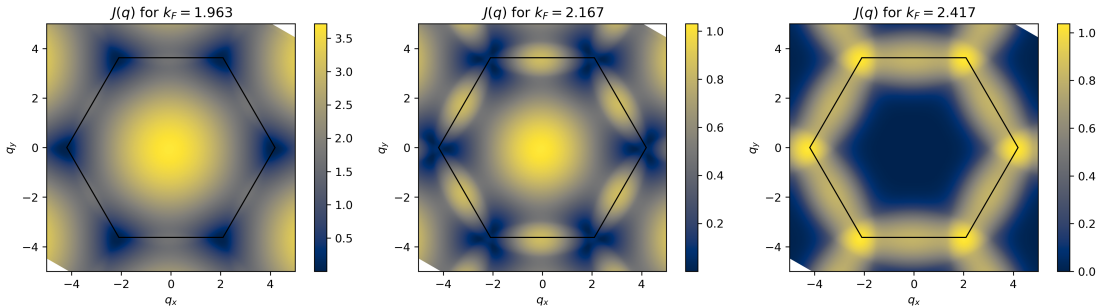

Figure 4.15: $J_{\vec{q}}$ for k_F equal to a)$\frac{2\pi}{3.2}$ b)$\frac{2\pi}{2.9}$ and c)$\frac{2\pi}{2.6}$, showing how $J_{\vec{q}}$ evolves from having minima at the K points, through having minima near the K points, and then to a very broad low-$J_{\vec{q}}$ region for larger k_F.

4.2.2 Results

We do the calculations for the RKKY crystal on a 300×300 system. We use J as our unit of energy, and the distance between lattice points a as our unit of length, meaning that we measure k_F in units of a^{-1}. When computing the free energy, the order parameter and T_c, we do the NBT calculations for 80 Δ's chosen on a logarithmic scale between 1 and 10^{-8}.

We start by considering a single value of $k_F = 2.32$. At this value, we are in the spiral phase, with the ordering vector being somewhere between the Γ point and the K point. There is a Z_3 nematic symmetry which can be broken.

First, we compute the free energy, which we see is multivalued in the region $0.0405 < T < 0.043$. By computing the order parameter, we see that it is zero above the multi-valued region and non-zero below, indicating that we do have a phase transition, and that this phase transition is related to the breaking of the Z_3 lattice symmetry. We can find the critical temperature by finding the place where the free energy branch associated with $I = 0$ crosses the one associated with $I \neq 0$. We find that this happens at $T_c = 0.042$. Looking at the structure factor above and below the phase transition, we clearly see that the Z_3 symmetry is broken below the critical temperature, where the structure factor only has inversion symmetry. By contrast, the high-temperature phase has both inversion symmetry and Z_3 symmetry, leading to a total of six peaks in the Brillouin zone. We also see that the peaks are broader in the high-temperature phase, indicating

that the thermal fluctuations are larger. From the structure factor, we can also see that the spiral phase found here is also found in triangular lattices with up to third-nearest neighbor couplings [12, 15].
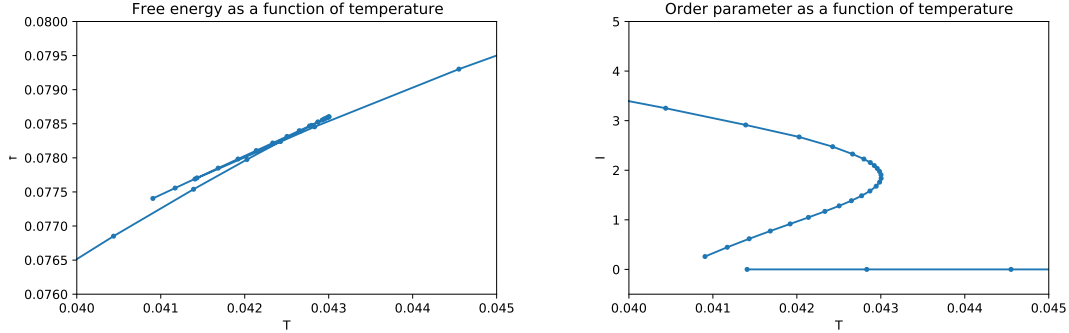

Figure 4.16: The free energy and order parameter for the RKKY crystal with $k_F = 2.32$. We see that they are both multivalued in the region $0.0405 < T < 0.043$. In this region, we have a phase transition.
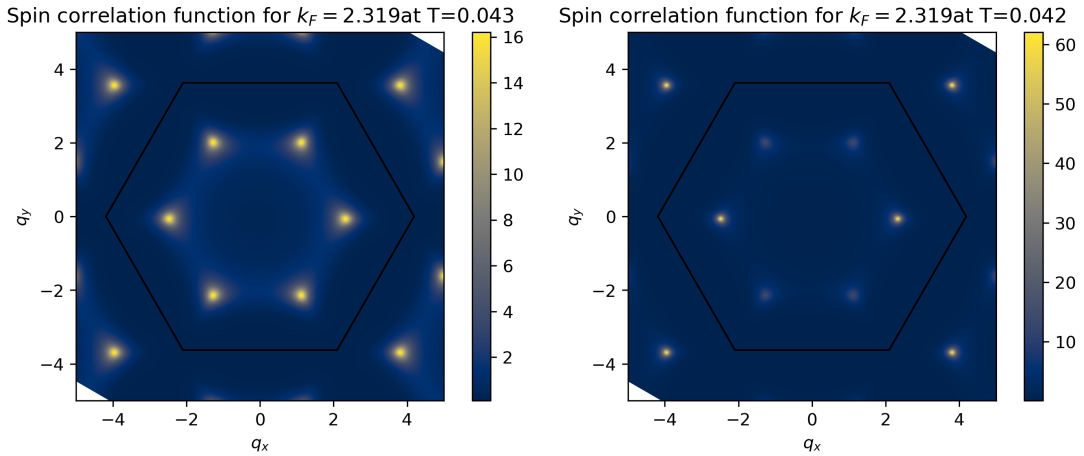

Figure 4.17: The structure factor at $T = 0.043$ and $T = 0.042$ for the $k_F = 2.32$ RKKY crystal. The high-T phase has sixfold symmetry, while the low-T phase only has twofold symmetry.

We see that for the high-temperature structure factor, the peaks are connected by lines of larger-valued structure factor. If we go near the nematic-ferromagnetic phase boundary at $k_F = 2.44$, we see that the connection between the peaks is very strong, and that a continuous ring is formed around the Γ point. We describe such a state as a modulated ring-liquid state, as the ring has maxima at the lines connecting the K point to the Γ point. Such a modulated ring liquid is also found in other spiral state regimes [12, 17]. As k_F changes, we go smoothly from the spiral paramagnetic state with fairly well-defined peaks, through a ring-liquid with soft peaks, and to a paramagnetic

state with a peak at the Γ point.
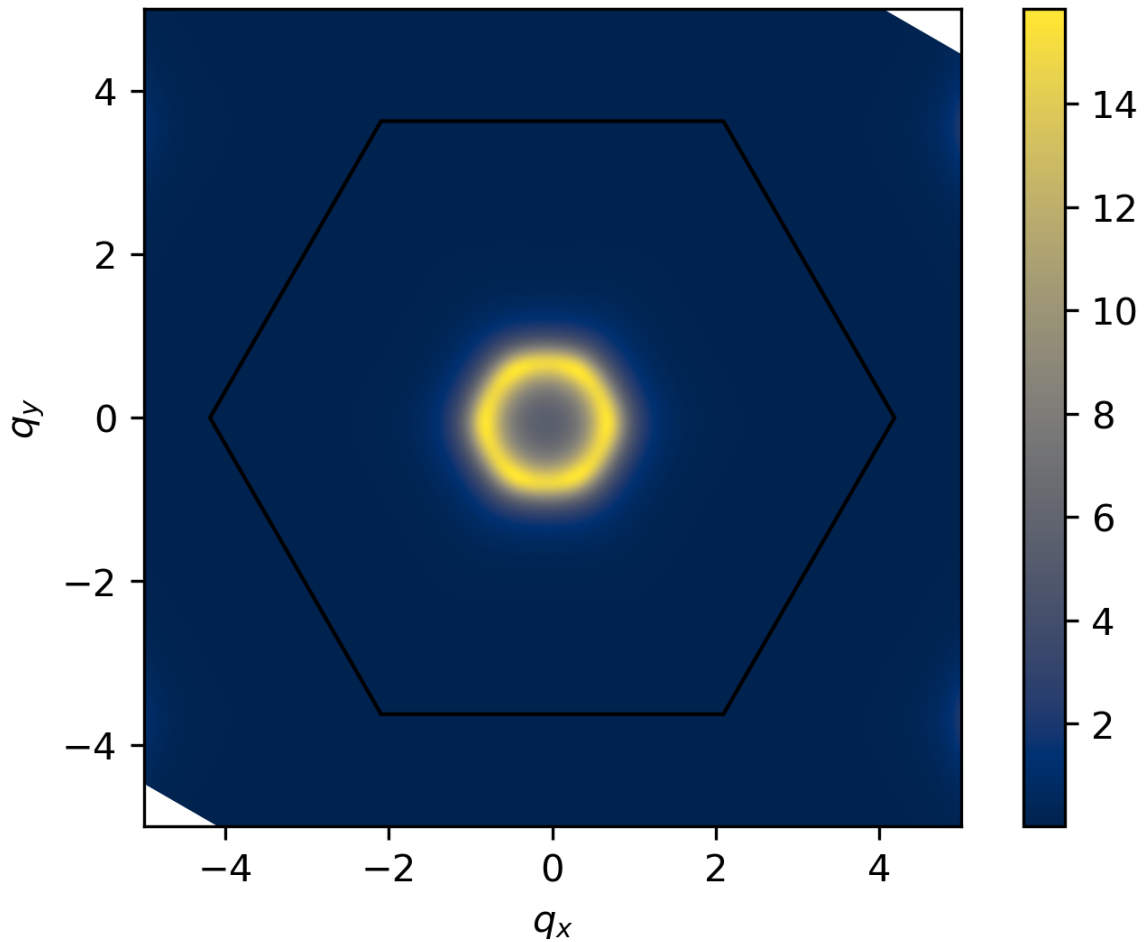
Figure 4.18: The structure factor for $k_F = \frac{2\pi}{2.6}$, showing the presence of a modulated ring around the Γ-point.

The structure factor in this ring-liquid region depends on the temperature. At high temperatures, the structure factor simply has a broad peak at the Γ point for $k_F = 2.42$. Lowering the temperature, a ring liquid develops before the nematic transition sets in. This behavior is very similar to what was found in [12] for a ring liquid on a honeycomb lattice.
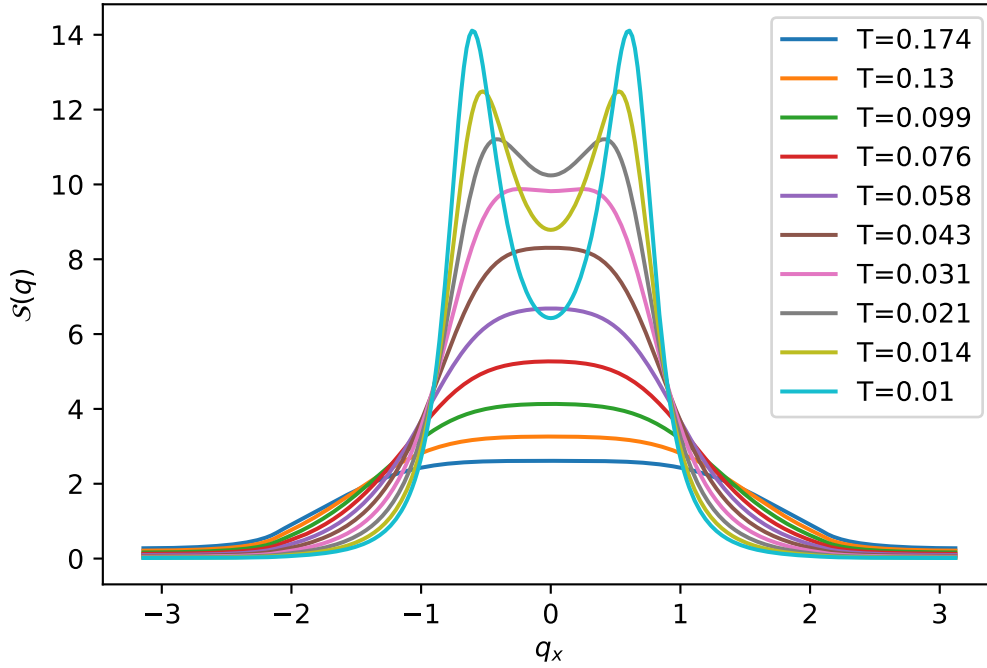
Figure 4.19: A cut through the structure factor at $(q_x, 0)$ at various temperature for $k_F = \frac{2\pi}{2.6}$, showing the development of a spin liquid (characterized by two peaks in this plot) at lower temperature

4.2.3 Critical temperature

Looking at the transition temperature in the nematic region, we see that just above $k_F = 2.11$, the transition temperature is fairly high at around 0.37. Increasing k_F further, the transition temperature decreases, and goes to zero as k_F nears 2.44. In the 120° region and the ferromagnetic region we do not observe a nematic transition.

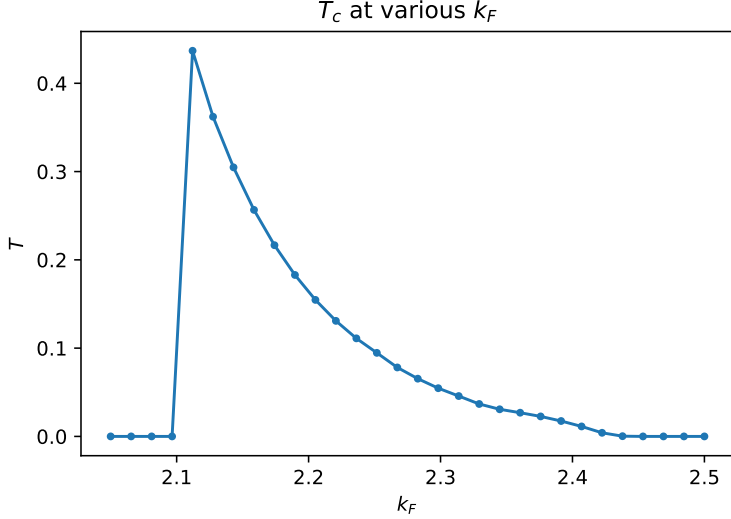Figure 4.20: Transition temperature for the RKKY crystal as a function of k_F. We see that the critical temperature is discontinuous at $k_F \approx 2.1$

The large T_c near the 120°-nematic phase transition is unexpected. In general, we would expect that the critical temperature is related to the energy barrier between the minima of J_q, as this determines whether the system can easily move between different minima. In this case, that doesn't appear to be the case, and the critical temperature is large even as the energy barrier between different minima is tiny. While we do not know why this phenomenon happens, we can conjecture that the effect is similar to that in order by disorder: While the energy barrier is small, the entropy change is large, and as such the free energy barrier is large.

As we saw, the heat capacity diverges at a phase transition. In a region with no phase transition, the heat capacity is smooth everywhere. we can see this by considering the system for $k_F = 1.93$, where we see a smooth specific heat curve with a broad maximum around $T = 1$. As we go to larger k_F, like 2.03, we see that this maximum becomes sharper and moves to a lower temperature of $T \approx 0.8$. We observe that as k_F nears the critical value of $k_F = 2.11$, the peak in the heat capacity sharpens and moves towards T_c at the critical k_F. We thus conjecture that this heat capacity peak has some link to the large critical temperature at low k_F.
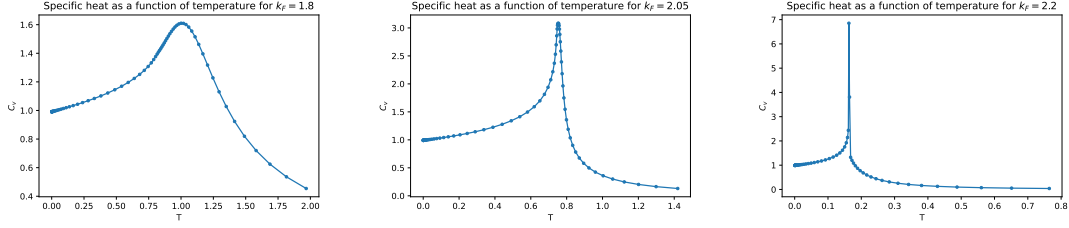
Figure 4.21: Heat capacity for a number of k_F. As k_F becomes larger, the peak in the heat capacity becomes sharper, and when k_F is large enough that a phase transition is possible, the heat capacity diverges.
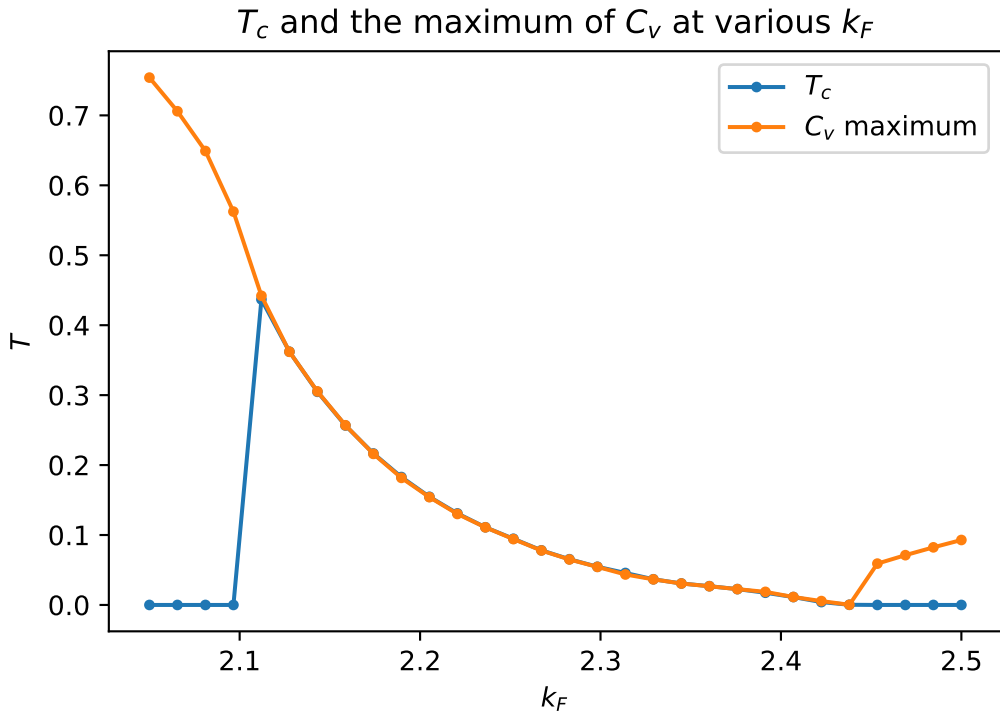
Figure 4.22: The critical temperature and the maximum of the specific heat for various k_F. When a phase transition is present, the maximum of the specific heat is always at the phase transition.

There has been no previous studies on the transition temperature of this model. As such, it is very hard to test how well NBT works on this model compared to Monte Carlo simulations. [29] computes the critical temperature for $k_F = 2.32$ and gets around 0.044, whereas we get 0.042, or about 5% less. This is unlike the case of exchange coupling, where NBT consistently gives a higher critical temperature. We attribute this difference to how we approximate the potential. At any rate, the difference is small enough that we can see some agreement between NBT and Monte Carlo. This, along with the fact that the phase transitions happen at the same k_F for NBT and for Monte Carlo indicates that

NBT does capture at least the qualitative behavior of the phase transition.

Looking at the phase diagram of the triangular lattice with up to third-nearest neigbor couplings, as explored with NBT in [15], we see that it also shows a transition between a 120° phase and a nematic phase. As such, we decide to explore this region further

4.2.4 High-temperature phase transition on triangular lattices

. The triangular $J_1 - J_2 - J_3$ model has a rich phase diagram. For $J_1 = -1$, one of the phase boundaries is between a nematic phase and a 120° phase. This happens somewhere in the region $J_3 > 1$, $J_2 < -\frac{1}{2}$, with the exact location of the phase boundary being some complex function of J_2 and J_3. As the nematic phase is also characterized by a $\vec{Q}$-vector lying on the line connecting the Γ point to the K point, this phase boundary appears to be very similar to the RKKY case, and as such exploring it may yield insights into the nature of the high-temperature phase transition in the RKKY crystal.

The J_1-J_2-J_3 model has the interaction matrix [15]

$$J_{\vec{q}} = 2J_3 A_{\vec{q}}^2 + (J_1 - 2J_3)A_{\vec{q}} + (J_2 - 2J_3)B_{\vec{q}} \tag{4.9}$$

where

$$A_{\vec{q}} = \cos(\vec{q} \cdot \vec{a}_1) + \cos(\vec{q} \cdot \vec{a}_2) + \cos(\vec{q} \cdot \vec{a}_3)$$
$$B_{\vec{q}} = \cos(\vec{q} \cdot (\vec{a}_1 + \vec{a}_2)) + \cos(\vec{q} \cdot (\vec{a}_2 + \vec{a}_3)) + \cos(\vec{q} \cdot (\vec{a}_3 - \vec{a}_1)) \tag{4.10}$$

with $\vec{a}_i$ defined as for the honeycomb lattice. With this interaction matrix, one can use NBT to compute the heat capacity and T_c of the system for various points in J_2-J_3 space. Specifically, we consider $J_2 = 1.5$, and look at a range of J_2. In this configuration, the system is 120° for large negative values of J_2, and in a nematic phase otherwise.
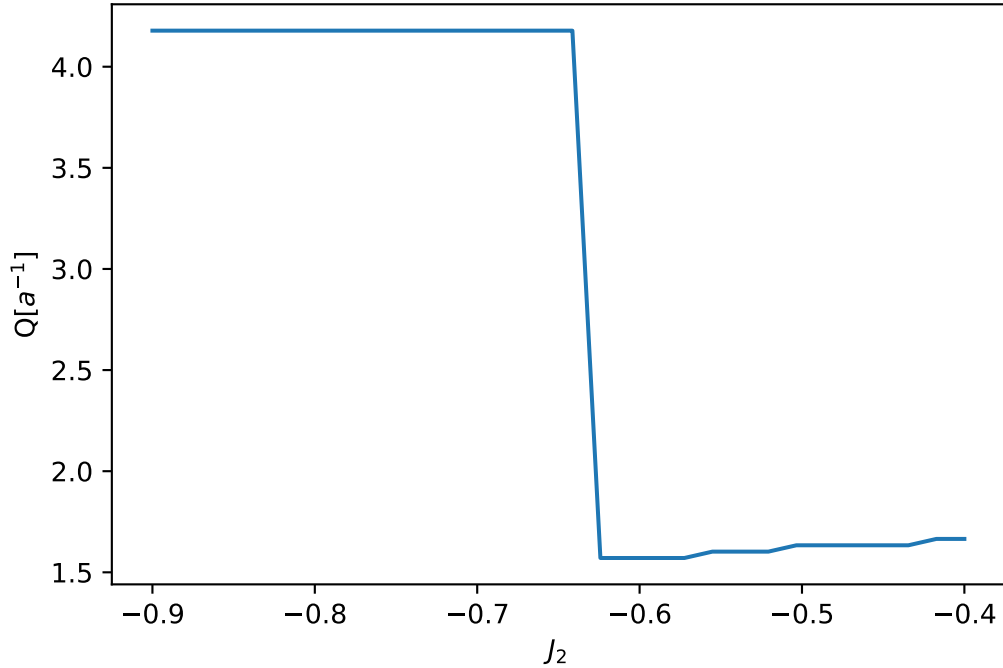
Figure 4.23: The ordering vector on the triangular lattice with $J_1 = -1$, $J_3 = 1.5$ as a function of J_2. The flat section indicates the 120° phase.

While this region contains a nematic-120° phase boundary, it is significantly different from the phase boundary in the RKKY crystal in one important way: The ordering vector changes discontinuously between a 120° ordering and a nematic ordering. This means that this change cannot be understood as a minimum moving around as we change J_2. Rather, we can understand this system as having a number of local minima, one of which becomes the global minimum depending on the value of J_2. Thus, we do not expect exactly the same behavior here as we do in the case of the RKKY crystal, but we are still interested in understanding the nature of the phase transition.
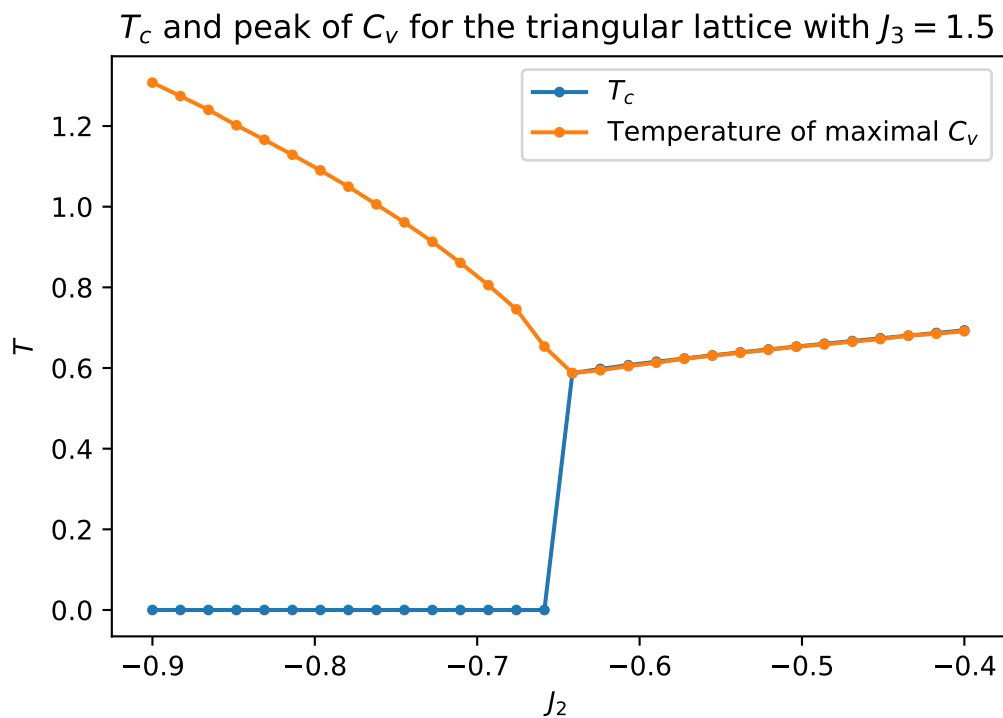
Figure 4.24: T_c and peak temperature of C_v for a range of J_2 for the $J_1 = -1, J_3 = 1.5$ triangular lattice.

Looking at the critical temperature and the temperature of the maximum of C_v, we see that while they do not behave exactly the same as in the case of the RKKY crystal, the heat capacity peak still moves towards the critical temperature at the phase boundary. Furthermore, looking at plots of the heat capacity for a number of values of J_2, we see the sharpening of the heat capacity peaks as we move towards the nematic-120° transition.
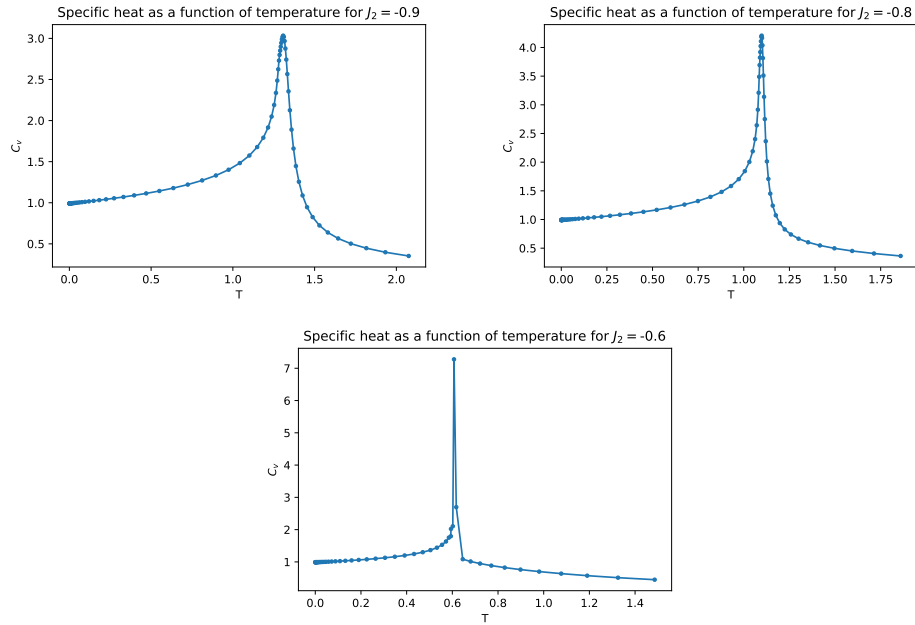
Figure 4.25: Specific heat plots for $J_2 = -0.9, -0.8$ and -0.6, showing how on the 120°
side of the transition, the peak in the heat capacity sharpens as we move towards the
phase boundary, and how the heat capacity diverges on the nematic side of the phase
boundary.

Chapter 5

Discussion

5.1 Vertex correction

When deriving NBT, we made an approximation of the self-energy and polarization, where we neglected the vertex correction. The vertex correction is the diagrams which renormalize the vertex the same way that the self-energy and polarization renormalizes the propagators. To see that the approximation is not exact, we can consider the self-energy. If we consider the approximation, the self-energy is

$$\text{(diagram)} = \text{(diagram)} + \text{(diagram)} + \text{(diagram)} + \mathcal{O}(1/N^3) \tag{5.1}$$

Meanwhile, the actual self-energy can be written as:

$$\Sigma_{\vec{q},ij} = \underbrace{\text{(diagram)}}_{\mathcal{O}(1/N)} + \underbrace{\text{(diagram)} + \text{(diagram)}}_{\mathcal{O}(1/N^2),\text{ no vertex correction}} + \underbrace{\text{(diagram)} + \text{(diagram)} + \text{(diagram)} + \text{(diagram)}}_{\mathcal{O}(1/N^2),\text{ vertex correction}} + \mathcal{O}(1/N^3) \tag{5.2}$$

We see that the majority of diagrams are not included in our approximation, which does call into question whether the approximation is valid. So far, the approximation has been used because it gives results which are similar to those found by Monte Carlo. Here, we are going to analyze the vertex correction in more detail to understand why neglecting it can be valid. If we start by considering a Bravais lattice, there is only one sublattice index and thus we can neglect it. We can thus define the dressed vertex as $\Gamma_{q,p}$ where q is the momentum of the incoming spin propagator and p is the momentum of the outgoing constraint propagator. We can write this to order $\mathcal{O}(1/N)$

$$\begin{array}{c} p \\ q \underset{}{\overset{}{\boxed{\Gamma}}} q-p \end{array} = \text{(diagram)} + \text{(diagram)} + \text{(diagram)} + \mathcal{O}(1/N^2) \tag{5.3}$$

We can then write

$$\Sigma_{\vec{q}} = (-i) \sum_{\vec{p}} \Gamma_{\vec{q},\vec{p}} D_{\vec{p}} K_{\text{eff}\,\vec{q}-\vec{p}}^{-1} = \quad \text{(5.4)}$$

and

$$D_{\vec{q}}^{-1} = i \sum_{\vec{p}} \Gamma_{\vec{p},-\vec{q}} K_{\text{eff}\,\vec{p}}^{-1} K_{\text{eff}\,\vec{q}+\vec{p}}^{-1} = \quad \text{(5.5)}$$

which are the exact equations for the self-energy and polarization. These equations are untenable to actually solve due to the fact that they cannot be solved by a convolution. As such, the sum needs to be carried out directly, which is very slow for large systems. Thus, for standard NBT the vertex corrections are neglected. The question is whether neglecting this correction is a problem. One way to analyze this is to compute the vertex correction to some order, and then compare it to the non-corrected values.

5.1.1 Computing the corrected self-energy

As we see in eq. (5.2), the majority of the diagrams for the self-energy up to $\mathcal{O}(1/N^2)$ are not included in NBT. Thus, we would like to see whether these diagrams are an important addition to the self-energy. Since these diagrams are relatively simple, it is computationally viable to simply calculate them and compare them to each other, at least if we choose a small enough lattice size. Specifically, if we consider a 10×10 lattice, we can compute these diagrams relatively quickly for both the square lattice and the triangular lattice. When comparing the NBT self-energy and the full self-energy, it is important to remember that in actual calculations, the minimal value of the self-energy is subtracted from the self-energy as one of the steps in the iteration. As such, it makes sense to define the magnitude of a self-energy as the difference between its maximal and minimal value, as this is the property which is actually computationally relevant.

Figure 5.1: The NBT self-energy, the full self-energy and the correction, plotted for next nearest neighbor couplings of $J_2 = 0.3$, 0.5 and 0.7 respectively on a square lattice with a nearest neighbor coupling of $J_1 = -1$. $J_2 = 0.5$ is the crossover between a ferromagnetic ground state and a nematic ground state.

Performing this calculation, we see that the difference in magnitude between the NBT self-energy and the full self-energy is tiny. In addition, we can see that the magnitude of
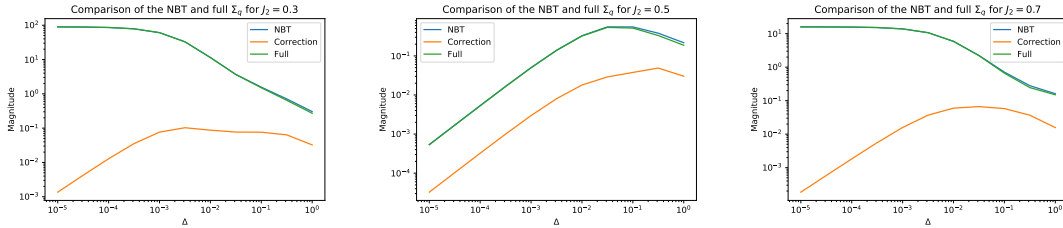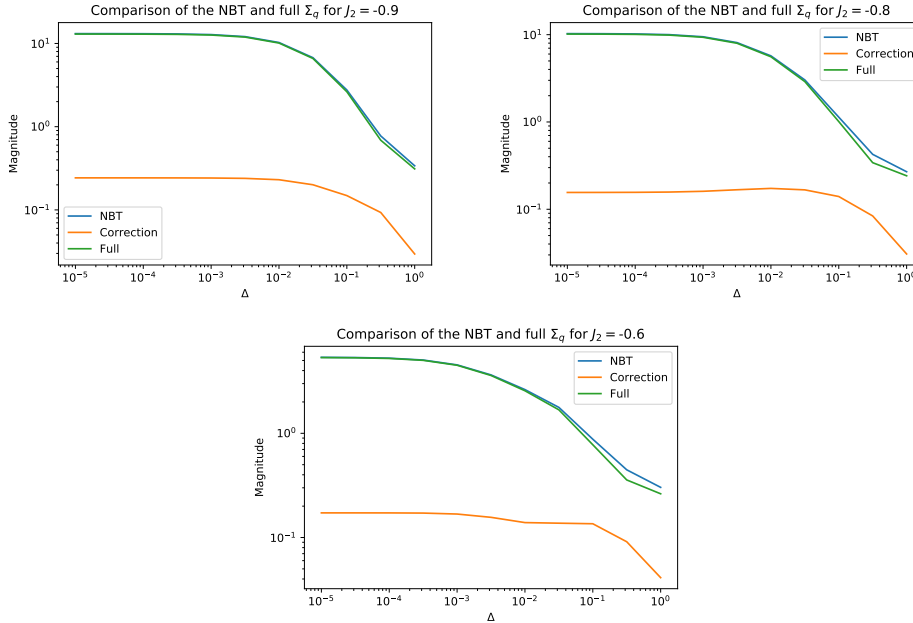
Figure 5.2: The NBT self-energy, the full self-energy and the correction, plotted for a next-nearest coupling of $J_3 = 1.5$ and nearest neigbor coupling of $J_1 = -1$ on a triangular lattice. These are the parameters also used to study the J_1-J_2-J_3 triangular lattice in this thesis.

the correction, which consists of all the diagrams not included in the NBT calculation, is also tiny. These two observations together show that the correction to the self-energy is small, at least to $\mathcal{O}(1/N^2)$, and can thus safely be ignored, at least for square and triangular lattices with short-range interactions.

We see here that the diagrams up to $\mathcal{O}(1/N^2)$ do not diverge as $\Delta \to 0$. In appendix B, we show that this holds for all diagrams.

5.1.2 Infinite-order considerations

When we do NBT we look at all orders, and certain traits like symmetry breaking are not found when simply looking at low-order diagrams. As such, one might ask whether the vertex correction matters for our infinite-order calculations. Of course, answering this would require us to perform NBT calculations with the vertex corrections, which is not feasible computationally. However, we can consider which approximations one could make to make this computation more feasible, and the consequences of these approximations.

One approximation schema which seems natural is to approximate the vertex correction as only depending on the momentum of the constraint propagator $\vec{p}$. Thus, the vertex can be written as $\Gamma_{\vec{q},\vec{p}} \to \Gamma_{\vec{p}}$. This approximation also holds if we can simply approximate Γ as a constant factor.

What we see is that, if our approximation of $\Gamma_{\vec{p},\vec{q}}$ is correct, the actual physics of the system are largely unchanged. To see this, let us compute the corrected constraint propagator and self-energy. The corrected constraint propagator now has the form

$$D_{\vec{q}}^{-1} = i\Gamma_{-\vec{q}} \sum_{\vec{p}} K_{\text{eff}\,\vec{p}}^{-1} K_{\text{eff}\,\vec{q}+\vec{p}}^{-1} \tag{5.6}$$

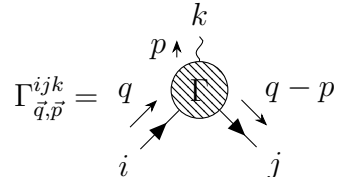which means that the self-energy has the form

$$\Sigma_{\vec{q}} = -i \sum_{\vec{p}} \Gamma_{\vec{p}} D_{\vec{p}} K_{\text{eff}\,\vec{q}-\vec{p}}^{-1} = -i \sum_{\vec{p}} \frac{\Gamma_{\vec{p}} K_{\text{eff}\,\vec{q}-\vec{p}}^{-1}}{i\Gamma_{-\vec{p}} \sum_{\vec{p}'} K_{\text{eff}\,\vec{p}'}^{-1} K_{\text{eff}\,\vec{p}+\vec{p}'}^{-1}}$$
$$= \sum_{\vec{p}} \frac{K_{\text{eff}\,\vec{q}-\vec{p}}^{-1}}{\sum_{\vec{p}'} K_{\text{eff}\,\vec{p}'}^{-1} K_{\text{eff}\,\vec{p}+\vec{p}'}^{-1}} = \sum_{\vec{p}} D_{\vec{p}} K_{\text{eff}\,\vec{q}-\vec{p}}^{-1}. \tag{5.7}$$

We thus see that the vertex correction doesn't factor into the self-energy, and as thus doesn't factor into K_{eff}, the structure factor or the temperature. It might factor into the free energy, which could matter in terms of the critical temperature. However, it can only change the critical temperature within the multivalued region, where different Δ's lead to the same T. As this region is tiny, the changes to the critical temperature are correspondingly tiny.

Of course, this argument only holds if the approximation of $\Gamma_{q,p}$ is good. However, combining it with the calculations of the corrected self-energy to $\mathcal{O}(1/N^2)$, it further constrains the effect of the vertex correction.
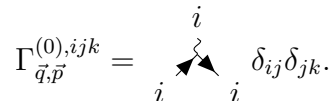
5.1.3 Non-Bravais lattice

All of the above considerations only applies to Bravais lattices, however. For non-Bravais lattices, the above argument fails, and indeed there is reason to believe that the vertex correction might have a greater effect. For a non-Bravais lattice, the vertex correction doesn't only change the numerical value of the vertex, it also changes the quantitative behavior of the vertex. To see this, we consider the dressed vertex

$$\Gamma_{\vec{q},\vec{p}}^{ijk} = \quad \begin{matrix} k \\ p \nearrow \\ q \nearrow \bigotimes \searrow q-p \\ \nearrow \quad \searrow \\ i \quad\quad j \end{matrix} \quad . \tag{5.8}$$

We note that it has three sublattice indices. If we only look at the bare part of the vertex, there is only one index

$$\Gamma_{\vec{q},\vec{p}}^{(0),ijk} = \quad \begin{matrix} i \\ \nwarrow \nearrow \\ i \quad i \end{matrix} \quad \delta_{ij}\delta_{jk}.$$

This means that in a sense, the bare interaction doesn't mix indices. The dressed interaction does, however, as we can see by looking at the diagrams to $\mathcal{O}(1/N)$

$$= \delta_{ij}\delta_{ik} \quad + \quad + \quad . \tag{5.9}$$

Since the propagators each mix sublattice indices, the diagrams which contains propagators have the opportunity to mix sublattices. This change can have a significant effect on the interaction. Unfortunately, it is also significantly harder to compute due to the fact that we now need to take care of many more indices.

The fact that the dressed vertex for non-Bravais lattices is qualitatively different from the bare vertex might help explaining the fact that the difference between NBT results and Monte Carlo results is significantly larger for the honeycomb lattice than for the triangular lattice [15]. In [15], it is proposed that this larger critical temperature is due to the fact that on $J_3 = 0$ line, the nematic transition happens in a region of continuously degenerate ground states, where the ordering vector is chosen through order by disorder. However, we propose that the significantly larger critical temperature is instead caused by not taking the vertex correction into account, and thus remains even when there is only a discrete set of ground states.

5.2   Specific heat

As we have seen, the specific heat found by NBT has a number of features that are not as expected from reading the litterature on magnetism. The first such feature is that $c_v \to m$ as $T \to 0$, where m is the number of sublattices. This is counter to the commonly known fact that in 3d magnetic systems, the specific heat goes as $T^{3/2}$ for small T [4]. The reason for this discrepancy is the various assumptions that go into the two computations: the $T^{3/2}$ law comes from a computation which is semi-classical in the sense that it does not consider quantum effects, but it does have quantized magnons. In a purely classical $O(n)$ theory, there is no quantization at all. We can thus compute the heat capacity in a way similar to how Boltzmann proved the Dulong-Petitt law for the heat capacity of a "classical" crystal [16].

We start by considering the partition function. At low T, we can assume that each spin is locally ordered around an axis which we call z for convenience, and that there are two excitations with quadratic dispersion for each spin. Thus, the partition function becomes:

$$Z \approx \prod_i \int d\delta S_{x,i} d\delta S_{y,i} e^{-\beta a (\delta S_{x,i}^2 + \Delta S_{y,i}^2)} \tag{5.10}$$

where a is some arbitrary constant and the product is over all atoms. These Gaussian integrals can then be performed to yield

$$Z = \prod_i \frac{\pi}{\beta a} = \left(\frac{\pi}{\beta a}\right)^N = \left(\frac{\pi T}{a}\right)^N \tag{5.11}$$

where N is the number of sites. This gives a free energy of

$$F = -T \ln(Z) = -NT \ln\left(\frac{\pi T}{a}\right), \tag{5.12}$$

and thus a heat capacity of

$$C_v = -T\frac{\partial^2 F}{\partial T^2} = N. \tag{5.13}$$

Thus, we see that the heat capacity at low temperatures is equal to the number of sites N, and as such the specific heat is equal to the number of sites per unit cell, which is equal to the number of sublattices. Knowing that the specific heat is equal to the number of sites doesn't just provide an explanation for the specific heat plots; it also provides a check to see whether all of the numerical factors in the solver program are correct. Specifically it helps ensure that the free energy is implemented properly, since numerical errors there could very well affect the specific heat.

5.3 Choosing Δ_i

To perform NBT calculations, we first have to choose the saddle point values of Δ_i. These values need to be chosen in such a way that the calculated temperature on each sublattice is the same. While the method for choosing Δ_i is not given by the theory, from a symmetry standpoint, simply choosing all of the Δ_i's to be equal seems like a good guess. Indeed, this method works well for the honeycomb lattice in most cases.

The method breaks on the honeycomb lattice when the inter-sublattice coupling is too small. To understand this, we can consider the case where the inter-sublattice coupling is zero. In that case, the two sublattices have nothing to do with each other, and should really be treated as two separate triangular lattices. When performing the NBT calculations, however, we subtract the minimal eigenvalue of $(\Sigma_{\vec{q},ij} + J_{\vec{q},ij})$. This minimal eigenvalue is simply the minimum of $(\Sigma_{\vec{q},11} + J_{\vec{q},11})$ or $(\Sigma_{\vec{q},22} + J_{\vec{q},22})$. This means that for one of the sublattices, we subtract the correct minimal eigenvalue, but for the other sublattice the wrong value gets subtracted. Thus, the calculations break down, and the temperatures on the two sublattices differ and do not converge.

Applying the same method to determine the Δ_i on a kagome lattice does not work, as the temperature on the different lattices is not the same no matter the coupling. Here, the sublattice symmetry seems to be broken by a more fundamental problem. To see this, we calculated the bare propagator $K_{\vec{q},ij}^{-1}$ for the kagome lattice with only nearest-neighbor

coupling, and thus only inter-lattice coupling. Of the nine sublattice elements of $K_{\vec{q},ij}$, 3 of them are the hermitian conjugate of 3 others due to inversion symmetry, while the diagonals are all simply Δ^{-1}. The three interesting elements are simply $120°$ rotations of each other. When $K_{\vec{q},ij}$ is inverted, however, the sublattice symmetry is broken. Looking at the diagonal $K_{\vec{q},ii}^{-1}$, this is identical for two of the sublattices but different for the third. One possible explanation is that inside each unit cell, two of the sublattices are related by a vector which is proportional to a lattice vector, while the third lattice is not related by such a vector. Thus, the numerics end up looking different, and this leads to an appreciable difference in the calculated results. Introducing an intra-sublattice coupling does not remedy the situation.

Considering this, it seems to suggest that NBT works well as long as the number of atoms in each unit cell is at most equal to the dimension of the lattice. While this describes many different crystals, it is a significant limit, especially because it does not include important frustrated lattices like the kagome (3 atoms in 2d) and pyrochlore (4 atoms in 3d).

5.4   RKKY crystal phase transition

The critical temperature for the RKKY crystal has a discontinuity at $k_F = 2.11$, where it goes from $T = 0$ to $T \approx 0.37$. At this k_F, the ordering vector goes from being at the K point to being at a non-symmetry point in the Brillouin zone. As such, it is not surprising that a phase transition does not happen for $k_F < 2.11$, but it is surprising that the critical temperature is so large near the critical k_F. Even so, this is also observed in other systems. As an example, the J_1-J_2-J_3 triangular system also exhibits a large critical temperature near the nematic-$120°$ phase boundary.

What makes the behavior at this phase boundary particularly surprising in the RKKY crystal is how it runs counter to the explanation of the critical temperature as being the temperature where the thermal fluctuations are large enough to cross the energy barrier. Near $k_F = 2.11$, the energy barrier between the ordering vectors is tiny, yet the critical temperature is relatively high. This is unlike in the case of the J_1-J_2-J_3 model, where the ordering vector changes discontinuously between a nematic and $120°$ ordering, and as such there is a relatively large energy barrier between the different nematic ordering vectors even near the phase boundary.

We observed that this high critical temperature on the nematic side of the critical point is related to a feature in the heat capacity on the $120°$ side, where the peak of the heat capacity sharpens as k_F nears the critical value. Exactly how this phenomenon is to be understood is unclear, but it does suggest that the high critical temperature is related to the overall physics of the system, and is not just an artifact. Again, this phenomenon is

also observed for the J_1-J_2-J_3 system.

It is natural to ask whether Nematic Bond Theory captures the fundamental features of systems with long-range interaction. Unfortunately, the very fact that NBT is better suited to this kind of problem when compared to Monte Carlo methods also mean that there are relatively few Monte Carlo studies of materials like the RKKY crystal. For the one k_F value where the phase transition has been calculated before, at $k_F = 2.32$, we get a critical temperature of $T_c = 0.042$, while [29] finds a critical temperature of around $T_c \approx 0.048$. The fact that NBT does not have exact agreement with Monte Carlo calculations is not surprising, but usually NBT reports larger critical temperatures than Monte Carlo. The fairly good agreement between the NBT value of T_c and the Monte Carlo value indicate that we are at least capturing some of the physics.

Even if we do not perfectly capture all of the physics of the RKKY crystal, we are still observing a strange phenomenon, where the critical temperature is very large compared to the energy barrier between $\vec{Q}$. The fact that such a transition is possible at all suggests that the main mechanism determining the critical temperature is not necessarily this energy barrier.

5.5   Spin liquid

When studying the RKKY crystal we observed that near the nematic-ferromagnetic phase boundary, the structure factor goes through three distinct forms. At high temperatures, there is a broad plateau centered at the Γ point. As the temperature is lowered, this continuously turns into a ring around Γ, before the nematic phase transition gives a structure factor with two peaks at low temperatures. This spin liquid behavior is very similar to what is observed in [12], where they looked at a honeycomb lattice with $J_2 = 0.183$. This similarity suggests a more general mechanism for understanding these "pancake liquids" and "ring liquids", as they are described in [12]. In both cases, $\vec{Q}$ is incommensurate but fairly close to a commensurate ordering vector. For the honeycomb case, there is a continuously degenerate ring of $\vec{Q}$-vectors, where the symmetry is broken through order by disorder. This is in contrast to the RKKY crystal, where there is a discrete set of $\vec{Q}$-vectors. Here, the ring is instead formed by a continuum of very low energy states.

The pancake and ring liquids have been explored by [30], who described this spin liquid from the basis of spiral states. In the spin liquid phase, the spins are locally described by a spiral state with an ordering vector $\vec{Q}$, but this local ordering vector fluctuates, and as such long-range order is broken. While their model captures the qualitative features of the spin liquid in the RKKY crystal, the RKKY crystal shows ordering at lower temperatures, and as such is not perfectly explained by their model.

5.6 Real magnetism

While Nematic Bond Theory is a very powerful theory for understanding the classical Heisenberg model, it has a number of limitations when applied to actual magnetic materials. One major limitation is that it only treats classical spins. In reality, all spins are quantum mechanical. As thus, it is worth considering whether our computations are actually applicable to real-world systems.

The most-commonly studied types of spins are classical vector spins like we do with NBT, and spin-$\frac{1}{2}$. Comparing the spin-$\frac{1}{2}$ honeycomb lattice to the classical vector version [31] shows that these two systems are radically different. When looking at the $J_1 - J_3$ honeycomb model, the two systems display completely different phases, with the quantum version never displaying an incommensurate spiral phase, and instead displaying types of order which cannot simply be represented with Villain's spiral ansatz eq.(2.3).

The reason for the large discrepancy between classical vector models and spin-$\frac{1}{2}$ models is that in general, the classical model is seen as a large-s model, which is applicable for large values of the quantum spin number. In this case, the many possible values of $\mathbf{S}_x$, $\mathbf{S}_y$ and $\mathbf{S}_z$ approach the continuum limit of simply representing it as a vector in an $O(3)$ model. This is not entirely true, however. While the dipole moment of a large-s spin does approximately behave like a classical vector, these spins also have higher-order terms like the quadropole moment. These are not treated at all by our vector model. Thus, the $O(3)$ model can be seen as a semi-classical version of the spin-$\frac{1}{2}$ model, and more complex models are required for higher spins [32].

While quadropolar terms and above do certainly exist, in practice the main type of interaction between magnetic moments is usually related to their dipoles, even if it is not a dipole-dipole magnetic interaction. As such, we are not particularly concerned with the fact that we might miss higher terms, although it is certainly worth keeping in mind when comparing NBT results to experiments.

Even in the large-s limit, our $O(3)$ model does not capture all of the features of real magnets. For example, the heat capacity of a real magnet goes to zero as $T \to 0$, while for an $O(3)$ model it goes to 1. Perhaps more important when comparing NBT to experimental results is the relatively limited form of the Hamiltonian. The Hamiltonian only contains one type of interaction, which can be written as $\vec{S} \cdot \vec{S}$. There are a number of important interactions, like the Dzyaloshinskii-Moriya interaction, which cannot be written in this form. In addition, NBT treats all spin dimensions as equal, and thus cannot account for anisotropic couplings. This is probably one of the most severe limitations of NBT, as anisotropic couplings are found in almost all materials.

We can still expect NBT to give approximate results for a number of materials, as long as those materials have low anisotropy and their magnetic moments are primarily interacting through the exchange interaction or the RKKY interaction. Although all materials

do have some anisotropy, in some materials the anisotropy is on a much lower energy scale than the spin-spin interaction, and as such one might be tempted to ignore it. It is worth noting that in the case of frustrated systems, while the interaction energy might be much higher than the anisotropy energy, the critical temperature can be on a comparable scale to the anisotropy, and as such we cannot simply ignore it. As thus, we need to be careful when comparing NBT results with real materials.

On the other hand, there is no reason that NBT is not comparable with Monte Carlo simulations. The major advantage of NBT compared to Monte Carlo is that NBT is much more efficient, and as such we can look at much larger systems. The ability to look at larger systems makes it easier to understand materials in which long-range interactions dominate. In addition, the efficiency of NBT means that several different values of the coupling constants can be analyzed quickly, and thus scanning large parts of the parameter space for interesting phases can be done with relative ease compared to Monte Carlo simulations.

Chapter 6

Conclusion

In this thesis, we have studied Nematic Bond Theory and its applications. In particular, we have studied the application of Nematic Bond Theory to systems with longer-range order than has been studied before. For the honeycomb lattice, we have extended NBT to third-nearest neighbor couplings. Here, we have found that nearest-neighbor and third-nearest neighbor couplings together lead to a system with varying degrees of frustration, and with a nematic phase transition whose temperature is proportional to $|J_3|$ for large values of J_3. Including second-nearest neighbor couplings opens up a large phase diagram, with different phase transitions showing different relations between T_c and the interaction strengths. We can thus see that the details of the nematic-non nematic phase boundary are not universal.

We have also studied the triangular lattice with an RKKY interaction. Here, we find that NBT approximately reproduces the results found by Monte Carlo methods inside the nematic phase. We have found evidence of spin liquid behaviour near the ferromagnetic-nematic phase boundary, and we have discovered an unusually high T_c at the 120°-nematic boundary. To further understand this, we have studied the behavior of a similar phase boundary in the triangular lattice with up to third-nearest neighbor couplings, and found a similarly high critical temperature. Although the details of the two systems vary in important ways, this demonstrates that this unusually high T_c is present in different systems, including systems which we know to be well-described by NBT. This high T_c, combined with the spin-liquid behavior, demonstrates the many complex properties of magnetic systems with long-range order.

We have also considered the theoretical footing of NBT. A key step in the derivation of NBT is the approximation that the vertex correction is negligible. Through direct calculation of the vertex correction up to $\mathcal{O}(1/N^2)$, we have shown that this is true on small lattices for the square and triangular lattices. We have also shown that this is true in general for Bravais lattices, assuming that the vertex correction only depends on the constraint field momentum. For non-Bravais lattices, we have described how the vertex

correction qualitatively changes the Feynman rules of the theory, and as such cannot be discounted as easily.

To further develop NBT as a computational tool, there are a number of hurdles which need to be overcome. The most severe is that NBT as it is currently formulated breaks down for complex non-Bravais lattices. While the exact details of this breakdown is unknown, we suggest that it happens when the number of sublattices is larger than the number of dimensions. Avoiding this breakdown is essential if NBT is to become a powerful tool for analyzing important frustrated systems like the kagome and pyrochlore lattices.

An additional key extension of NBT is the inclusion of external magnetic fields. Currently, NBT is defined without any external magnetic fields. Extending NBT to include external magnetic fields would necessitate a re-derivation of the field theory while including a magnetic term in the Hamiltonian. The nature of how such a magnetic field would change the theoretical aspects of NBT are unclear, but it would most likely require separate treatment of the different spin components, which in turn changes the $1/N$ expansion.

Considering the results acquired in this thesis, it is clear that the RKKY crystal hosts interesting physical phenomena. Further studies of that system, either with NBT, Monte Carlo methods or other methods could potentially yield insights into the behavior of frustrated magnetic systems in general. In particular, the nature of the high T_c near the phase boundary is not well-understood. Although similar behavior has been found in systems with shorter-range couplings, the details of the RKKY crystal means that the high T_c is particularly strange, and as such understanding it would greatly expand on our understanding of the nematic transition in frustrated magnets.

Bibliography

[1] L. Balents, "Spin liquids in frustrated magnets," *Nature*, vol. 464, pp. 199–208, Mar. 2010.

[2] O. F. Syljuåsen, J. Paaske, and M. Schecter, "Interplay between magnetic and vestigial nematic orders in the layered J 1 − J 2 classical Heisenberg model," *Physical Review B*, vol. 99, p. 174404, May 2019.

[3] C. J. Foot, *Atomic Physics*. Oxford Master Series in Physics, Oxford: Oxford University Press, 2005.

[4] S. Blundell, *Magnetism in Condensed Matter*. Oxford Master Series in Condensed Matter Physics, Oxford University Press, 2001.

[5] D. S. Inosov, D. V. Evtushinsky, A. Koitzsch, V. B. Zabolotnyy, S. V. Borisenko, A. A. Kordyuk, M. Frontzek, M. Loewenhaupt, W. Löser, I. Mazilu, H. Bitterlich, G. Behr, J.-U. Hoffmann, R. Follath, and B. Büchner, "Electronic Structure and Nesting-Driven Enhancement of the RKKY Interaction at the Magnetic Ordering Propagation Vector in Gd 2 PdSi 3 and Tb 2 PdSi 3," *Physical Review Letters*, vol. 102, p. 046401, Jan. 2009.

[6] E. Ressouche, V. Simonet, B. Canals, M. Gospodinov, and V. Skumryev, "Magnetic Frustration in an Iron-Based Cairo Pentagonal Lattice," *Physical Review Letters*, vol. 103, p. 267204, Dec. 2009.

[7] K. Takubo, T. Mizokawa, J.-Y. Son, Y. Nambu, S. Nakatsuji, and Y. Maeno, "Unusual Superexchange Pathways in an NiS 2 Triangular Lattice with Negative Charge-Transfer Energy," *Physical Review Letters*, vol. 99, p. 037203, July 2007.

[8] N. D. Mermin and H. Wagner, "Absence of ferromagnetism or antiferromagnetism in one- or two-dimensional isotropic heisenberg models," *Phys. Rev. Lett.*, vol. 17, pp. 1133–1136, Nov 1966.

[9] J. Villain, "A magnetic analogue of stereoisomerism : application to helimagnetism in two dimensions," *Journal de Physique*, vol. 38, no. 4, pp. 385–391, 1977.

[10] C. L. Henley, "Ordering due to disorder in a frustrated vector antiferromagnet," *Physical Review Letters*, vol. 62, pp. 2056–2059, Apr. 1989.

[11] C. L. Henley, "The "Coulomb Phase" in Frustrated Systems," *Annual Review of Condensed Matter Physics*, vol. 1, pp. 179–210, Aug. 2010.

[12] S. Okumura, H. Kawamura, T. Okubo, and Y. Motome, "Novel Spin-Liquid States in the Frustrated Heisenberg Antiferromagnet on the Honeycomb Lattice," *Journal of the Physical Society of Japan*, vol. 79, p. 114705, Nov. 2010.

[13] O. Gauthé and F. Mila, "Thermal Ising Transition in the Spin- 1 / 2 J 1 - J 2 Heisenberg Model," *Physical Review Letters*, vol. 128, p. 227202, June 2022.

[14] D. A. Garanin, "Self-Consistent Gaussian Approximation for Classical Spin Systems: Thermodynamics," *Physical Review B*, vol. 53, pp. 11593–11605, May 1996. arXiv:cond-mat/9804040.

[15] C. Glittum, "Nematic Bond Theory of Frustrated Heisenberg Models on Triangular and Honeycomb Lattices," Master's thesis, University of Oslo, 2020.

[16] S. H. Simon, *The Oxford Solid State Basics.* Oxford University Press, 2013.

[17] C. Glittum and O. F. Syljuåsen, "Arc-shaped structure factor in the J 1 − J 2 − J 3 classical Heisenberg model on the triangular lattice," *Physical Review B*, vol. 104, p. 184427, Nov. 2021.

[18] A. R. Wildes, J. R. Stewart, M. D. Le, R. A. Ewings, K. C. Rule, G. Deng, and K. Anand, "Magnetic dynamics of NiPS 3," *Physical Review B*, vol. 106, p. 174422, Nov. 2022.

[19] A. R. Wildes, B. Fåk, U. B. Hansen, M. Enderle, J. R. Stewart, L. Testa, H. M. Rønnow, C. Kim, and J.-G. Park, "Spin wave spectra of single crystal CoPS$_3$," Dec. 2022. arXiv:2212.06479 [cond-mat].

[20] E. Ergeçen, B. Ilyas, J. Kim, J. Park, M. B. Yilmaz, T. Luo, D. Xiao, S. Okamoto, J.-G. Park, and N. Gedik, "Coherent detection of hidden spin-lattice coupling in a van der Waals antiferromagnet," *Proceedings of the National Academy of Sciences*, vol. 120, p. e2208968120, Mar. 2023. arXiv:2303.05963 [cond-mat].

[21] J. Fouet, P. Sindzingre, and C. Lhuillier, "An investigation of the quantum J 1 - J 2 - J 3 model on the honeycomb lattice," *The European Physical Journal B*, vol. 20, pp. 241–254, Mar. 2001.

[22] L. Messio, C. Lhuillier, and G. Misguich, "Lattice symmetries and regular magnetic orders in classical frustrated antiferromagnets," *Physical Review B*, vol. 83, p. 184401, May 2011.

[23] A. Mulder, R. Ganesh, L. Capriotti, and A. Paramekanti, "Spiral order by disorder and lattice nematic order in a frustrated Heisenberg antiferromagnet on the honeycomb lattice," *Physical Review B*, vol. 81, p. 214419, June 2010. arXiv:1004.1119 [cond-mat].

[24] C. Weber, L. Capriotti, G. Misguich, F. Becca, M. Elhajal, and F. Mila, "Ising Transition Driven by Frustration in a 2D Classical Model with Continuous Symmetry," *Physical Review Letters*, vol. 91, p. 177202, Oct. 2003.

[25] J. Rehn, A. Sen, K. Damle, and R. Moessner, "Classical Spin Liquid on the Maximally Frustrated Honeycomb Lattice," *Physical Review Letters*, vol. 117, p. 167201, Oct. 2016.

[26] S. R. Saha, H. Sugawara, T. D. Matsuda, H. Sato, R. Mallik, and E. V. Sampathkumaran, "Magnetic anisotropy, first-order-like metamagnetic transitions, and large negative magnetoresistance in single-crystal Gd 2 PdSi 3," *Physical Review B*, vol. 60, pp. 12162–12165, Nov. 1999.

[27] T. Kurumaji, T. Nakajima, M. Hirschberger, A. Kikkawa, Y. Yamasaki, H. Sagayama, H. Nakao, Y. Taguchi, T.-h. Arima, and Y. Tokura, "Skyrmion lattice with a giant topological Hall effect in a frustrated triangular-lattice magnet," *Science*, vol. 365, pp. 914–918, Aug. 2019.

[28] A. Szytuła, M. Hofmann, B. Penc, M. Ślaski, S. Majumdar, E. V. Sampathkumaran, and A. Zygmunt, "Magnetic behaviour of R2PdSi3 compounds with R=Ce,Nd,Tb–Er," *Journal of Magnetism and Magnetic Materials*, vol. 202, no. 2, pp. 365–375, 1999.

[29] K. Mitsumoto and H. Kawamura, "Skyrmion crystal in the RKKY system on the two-dimensional triangular lattice," *Physical Review B*, vol. 105, p. 094427, Mar. 2022. arXiv:2112.06414 [cond-mat].

[30] H. Yan and J. Reuther, "Low-energy structure of spiral spin liquids," *Physical Review Research*, vol. 4, p. 023175, June 2022.

[31] S. Jiang, S. R. White, and A. L. Chernyshev, "Quantum Phases in the Honeycomb-Lattice J_1–J_3 Ferro-Antiferromagnetic Model," Apr. 2023. arXiv:2304.06062 [cond-mat].

[32] K. Remund, R. Pohle, Y. Akagi, J. Romhányi, and N. Shannon, "Semi-classical simulation of spin-1 magnets," *Physical Review Research*, vol. 4, p. 033106, Aug. 2022.

Appendix A

Fourier conventions

We use a number of different Fourier conventions in this thesis to maximally simplify our equations. As the thesis is largely numerical in nature, all of our Fourier transforms are discrete. For the spins, we use the convention

$$\vec{S}_{\vec{r},i} = \frac{1}{\sqrt{V}} \sum_{\vec{q}} \vec{S}_{\vec{q},i} e^{i\vec{q}\cdot\vec{r}} \qquad \vec{S}_{\vec{q},i} = \frac{1}{\sqrt{V}} \sum_{\vec{r}} \vec{S}_{\vec{r},i} e^{-i\vec{q}\cdot\vec{r}} \tag{A.1}$$

and similarly for the constraint field

$$\lambda_{\vec{r},i} = \frac{1}{\sqrt{V}} \sum_{\vec{q}} \lambda_{\vec{q},i} e^{i\vec{q}\cdot\vec{r}} \qquad \lambda_{\vec{q},i} = \frac{1}{\sqrt{V}} \sum_{\vec{r}} \lambda_{\vec{r},i} e^{-i\vec{q}\cdot\vec{r}}. \tag{A.2}$$

For the spin-spin coupling, we use a different convention to ensure the simplicity of the equations:

$$J_{\vec{r},i} = \frac{2}{V} \sum_{\vec{q}} J_{\vec{q},i} e^{i\vec{q}\cdot\vec{r}} \qquad J_{\vec{q},i} = \frac{1}{2} \sum_{\vec{r}} J_{\vec{r},i} e^{-i\vec{q}\cdot\vec{r}} \tag{A.3}$$

These conventions are the ones that lead to the fewest extra factors when moving between reciprocal space and real space.

Appendix B

Self-energy divergence in Δ

We want to show that none of the self-energy diagrams diverge as $\Delta \to 0$. We can start by seeing why this is a potential problem: The bare spin propagator is given by $K_{\vec{q}}^{-1} = (J_{\vec{q}} + \Delta)^{-1}$, and for the ordering vector $\vec{Q}$, $J_{\vec{Q}} = 0$ and thus $K_{\vec{Q}}^{-1} = \Delta^{-1}$. Thus, we might worry that diagrams grow larger and larger for smaller Δ. To see why this is not a problem, we consider the small Δ limit, and count powers of Δ. Let us define $\vec{q} \neq \vec{Q}$ as a non-ordering vector. We then get $K_{\vec{q}}^{-1} \propto 1$ and $K_{\vec{Q}}^{-1} \propto \Delta^{-1}$. We can now look at the constraint propagator:

$$D_{0,\vec{q}} = \frac{2}{N} \left[\sum_{\vec{p}} K_{\vec{p}}^{-1} K_{\vec{q}-\vec{p}}^{-1} \right]^{-1} \tag{B.1}$$

We see that for small Δ, the dominant terms of $\sum_{\vec{p}} K_{\vec{p}}^{-1} K_{\vec{q}-\vec{p}}^{-1}$ are $K_{\vec{Q}}^{-1} K_{\vec{q}-\vec{Q}}^{-1}$ and $K_{\vec{Q}-\vec{q}}^{-1} K_{\vec{Q}}^{-1}$. Each of these terms carry a factor of Δ^{-1}, so we usually get $D_{0,\vec{q}} \propto \Delta$. However, if $\vec{q} - \vec{Q}$ or $\vec{Q} - \vec{q}$ are also ordering vectors, then these terms carry a factor Δ^2. We define $\vec{k}$ as a momentum such that $\vec{k} - \vec{Q}$ or $\vec{Q} - \vec{k}$ are ordering vectors(Since we assume inversion symmetry, $\vec{k} - \vec{Q}$ being an ordering vector implies that $\vec{Q} - \vec{k}$ is an ordering vector.) We thus have four types of objects in our diagrams:

- $x = K_{\vec{q}}^{-1}$, which carry no Δ-dependence

- $X = K_{\vec{Q}}^{-1}$, which are proportional to Δ^{-1}

- $y = D_{\vec{q}}$, which are proportional to Δ

- $Y = D_{\vec{k}}$, which are proportional to Δ^2

Our diagrams consist of a spin propagator which is not closed, a number of closed spin loops, and constraint propagators connecting them. As each constraint propagator connects two objects, it makes sense to define the ends of the constraint propagators as l for the y-propagator and L for the Y-propagator. We see that $l \propto \Delta^{1/2}$ and $L \propto \Delta$.

B.1 Cases

To actually show that these diagrams do not diverge with Δ, we will analyze a number of cases. In each case, we will construct the diagram with the lowest power of Δ, and show that it does not diverge as $\Delta \to 0$. We will index our cases by the number of l and L they contain.

Starting with the single open propagator, we define a (m, n) propagator as one containing m l-terms and n L-terms. We now want to construct the lowest-order (m, n) propagators, which means the ones with the most X terms. We note that the possible connections are xlx, Xlx, xlX, XLX and xLx. If we start with $n = 0$, the lowest order diagrams are:

$$
(x) \underbrace{LxLxLx...L}_{m}(x) \propto \Delta^m
$$
$$
(X) \underbrace{LXLXLX...L}_{m}(X) \propto \Delta^1
$$
(B.2)

Where the terms in parentheses are the external momenta, which are fixed and do not contribute powers. For n even, the optimal constructions are:

$$
(x)lX \underbrace{LXLX...LX}_{m} \underbrace{lxlXlxlXl}_{n-1}(x) \propto \Delta^0
$$
$$
(X) \underbrace{LXLX...LX}_{m} \underbrace{lxlXlxl}_{n}(X) \propto \Delta^1
$$
(B.3)

Whereas for n odd, the optimal constructions are

$$
(x)lX \underbrace{LXLXLX}_{m} \underbrace{lxlXlxl}_{n-1}(x) \propto \Delta^{1/2}
$$
$$
(X) \underbrace{LXLXLX}_{m} \underbrace{lxlXlxlxl}_{n-1}(X) \propto \Delta^{3/2}
$$
(B.4)

We thus see that all of the open propagators are well-controlled.

For the loops, a very similar logic goes. We can construct the loops by closing these open propagators. For the porpagators with (x) at the end, closing them does not alter their divergene properties. Closing the propagators with a (X) at the ends adds a factor of Δ, but in none of the cases does this bring them above Δ^0. Thus, we can see that no diagram diverges when $\Delta \to 0$.

Appendix C

Implementation of NBT

The numerical code used to perform NBT computations was written in Python with the numpy and scipy libraries. The plots were produced with the matplotlib library. As a concrete example, an example of the code used to create a plot of the structure factor for a honeycomb lattice is provided. It is important to note that line 24 is split in two due to its length; when implementing this code it is important to keep it as one line.

```python
1   import numpy as np
2   import matplotlib.pyplot as plt
3   import scipy
4   import matplotlib.patches as patch
5
6   Size=200
7   t_1=np.array([1,0])
8   t_2=np.array([1/2,np.sqrt(3)/2])
9   t_3=t_2-t_1
10  v_dist=[[[0,0],[0,np.sqrt(3)/3]],[[0,-np.sqrt(3)/3],[0,0]]]
11
12  J_1=1
13  J_2=0
14  J_3=-0.5
15  x=np.linspace(0,1,Size,endpoint=False)
16  y=x
17  q1,q2=np.meshgrid(x,y)
18  qx=2*np.pi*q1
19  qy=2*np.pi*(1/np.sqrt(3)*q1+2/np.sqrt(3)*q2)
20  q_vec=np.array([qx,qy])
21  q_vec=np.moveaxis(q_vec,0,2)
22  def J_func(q_vec):
23      J_aa=J_2*(np.cos(np.dot(q_vec,t_1))+np.cos(np.dot(q_vec,t_2))+np.cos(np.dot(q_vec,t_3)))
24      J_ab=1/2*J_1*(1+np.exp(1j*np.dot(q_vec,-t_2))+np.exp(1j*np.dot(q_vec,-t_3)))+1/2*J_3*(np.exp(1j*np.dot(q_vec,t_1))+np.exp
            (1j*np.dot(q_vec,-t_1))+np.exp(1j*np.dot(q_vec,-t_2-t_3)))
25      J_ba=J_ab.conj()
26      J_bb=J_aa
27      return np.moveaxis(np.array([[J_aa,J_ab],[J_ba,J_bb]]),[-2,-1],[0,1])
28
29  #Conventions: objects are in reciprocal space unless specified, [0,0] marks the center of the first Brillouin zone.
30  #Indices go [q1,q2,i,j] for 4d objects
31  #The convention for the sign of Sigma is that used in the computation part of the thesis
32  Delta=1e-1
33  #Initialize the program
34  Volume=Size**2
35  sublatticeI=np.tensordot(np.ones((Size,Size)),np.identity(2),axes=0)
36  #Define Fourier transformation and matrix operations.
37  def fourier(M):
38      return scipy.fft.fftn(M,axes=(0,1))/Volume*2/np.sqrt(3)
39  def invfourier(M):
40      return Volume*scipy.fft.ifftn(M,axes=(0,1))*np.sqrt(3)/2
41  def eigenvalues(M):
42      return np.linalg.eigvals(M)
43  def hermitian(M):
44      return np.transpose(M,axes=(0,1,3,2)).conj()
```

```
45
46    #Helper functions
47    def period_expander(M):
48        M_c=M
49        return np.concatenate((np.concatenate((M_c,M_c),axis=0),np.concatenate((M_c,M_c),axis=0)),axis=1)
50    #Create array J from J_func reasonably efficiently
51    J=J_func(q_vec)
52    J_min=np.amin(eigenvalues(J))
53    J=J-sublatticeI*J_min
54
55
56    Sigma_init=np.random.rand(Size,Size,2,2)*0.0001*Delta
57    Sigma=fourier(Sigma_init)
58    Sigma=(Sigma+hermitian(Sigma))/2
59    #Sigma=np.zeros((Size,Size,2,2))
60    T=np.ones((2))*float("nan")
61
62    #iterations
63    Brokenloop=False
64    iterations=0
65    while Brokenloop==False:
66        #1
67        Sigma_min=np.amin(eigenvalues(Sigma+J))
68        Sigma=Sigma-Sigma_min*sublatticeI
69        #2
70        K_effinv=np.linalg.inv((J+Delta*sublatticeI+Sigma))
71        T_old=T
72        T=np.diag(1/(3/(2*Volume)*np.sum(K_effinv,axis=(0,1)).real))
73        if np.all(abs((T-T_old)/T_old)<1e-10):
74            print("Converged")
75            print(iterations)
76            break
77        elif iterations>200:
78            print("Too many iterations")
79            Brokenloop=True
80        #3
81        D_inv=3/2*fourier(invfourier(K_effinv)**2)
82        #4
83        D_calc=np.linalg.inv(D_inv)
84        D_calc[0,0]=np.zeros((2,2))
85        Sigma=fourier((invfourier(K_effinv)*invfourier(D_calc)).real)
86        iterations+=1
87        print(T)
88    Sigma=(Sigma+hermitian(Sigma))/2
89    #Structure factor calculation
90    def struc(K):
91        x_large=np.concatenate((x-2,x-1,x,x+1))
92        y_large=x_large
93        q1_large,q2_large=np.meshgrid(x_large,y_large)
94        qxl=2*np.pi*q1_large
95        qyl=2*np.pi*(1/np.sqrt(3)*q1_large+2/np.sqrt(3)*q2_large)
96        q_vec_large=np.array([qxl,qyl])
97        q_vec_large=np.moveaxis(q_vec_large,0,2)
98        expfactor=np.exp(np.tensordot(q_vec_large,v_dist,axes=[[2],[2]])*1j)
99        K_expanded=period_expander(period_expander(K))
100       return np.sum(expfactor*K_expanded,axis=(2,3))*T[0]*3/2,qxl,qyl
101   S,Sqx,Sqy=struc(K_effinv)
102   nplot=plt.scatter(Sqx,Sqy,c=(abs(S)),marker=".",s=1)
103   plt.gca().set_aspect('equal', adjustable='box')
104   ax=plt.gca()
105   hpatch2=patch.RegularPolygon(q_vec[0,0],6,4*np.pi/3,orientation=np.pi/6,facecolor="None",edgecolor="black")
106   hpatch3=patch.RegularPolygon(q_vec[0,0],6,7*np.pi/3,facecolor="None",edgecolor="black")
107   ax.add_patch(hpatch2)
108   ax.add_patch(hpatch3)
109   plt.xlim(-3*np.pi,3*np.pi)
110   plt.ylim(-3*np.pi,3*np.pi)
111   plt.xlabel("$q_{x}$")
112   plt.ylabel("$q_{y}$")
113   plt.title("$\mathcal{S}(\mathbf{q})$ for $J_{1}$="+str(J_1)+", $J_{3}$="+str(J_3)+", T=" + str(round(T[0],3)))
114   plt.show()
```

74